Coastal Perturbations of Marine-Layer Winds, Wind Stress, and Wind Stress Curl along California and Baja California in June 1999

DARKO KORAČIN

Desert Research Institute, Reno, Nevada

CLIVE E. DORMAN

Scripps Institution of Oceanography, La Jolla, and San Diego State University, San Diego, California

EDWARD P. DEVER

Scripps Institution of Oceanography, La Jolla, California

(Manuscript received 29 April 2003, in final form 9 October 2003)

ABSTRACT

Month-long simulations using the fifth-generation Pennsylvania State University–National Center for Atmospheric Research Mesoscale Model (MM5) with a horizontal resolution of 9 km have been used to investigate perturbations of topographically forced wind stress and wind stress curl during upwelling-favorable winds along the California and Baja California coasts during June 1999. The dominant spatial inhomogeneity of the wind stress and wind stress curl is near the coast. Wind and wind stress maxima are found in the lees of major capes near the coastline. Positive wind stress curl occurs in a narrow band near the coast, while the region farther offshore is characterized by a broad band of weak negative curl. Curvature of the coastline, such as along the Southern California Bight, forces the northerly flow toward the east and generates positive wind stress curl even if the magnitude of the stress is constant. The largest wind stress curl is simulated in the lees of Point Conception and the Santa Barbara Channel. The Baja California wind stress is upwelling favorable. Although the winds and wind stress exhibit great spatial variability in response to synoptic forcing, the wind stress curl has relatively small variation. The narrow band of positive wind stress curl along the coast adds about 5% to the coastal upwelling generated by adjustment to the coastal boundary condition. The larger area of positive wind stress curl in the lee of Point Conception may be of first-order importance to circulation in the Santa Barbara Channel and the Southern California Bight.

1. Introduction

The importance of winds, wind stress, and wind stress curl in driving ocean dynamics is well known; however, the accuracy of estimates of spatial and temporal characteristics is significantly limited by a lack of observations over the ocean. In the late 1970s the problem of accurate estimates of wind stress in coastal regions was recognized and elaborated on by Nelson (1977). Significant advances in understanding the structure of wind stress and wind stress curl came from direct measurements of near-surface winds and wind stress using instrumented aircraft (Caldwell et al. 1986; Beardsley et al. 1987; Enriques and Friehe 1995, 1997; Rogers et al. 1998; Dorman et al. 1999). By the late 1990s, satellite microwave instruments generated surface wind estimates with a horizontal resolution of about 0.25°, but measurement errors require heavy filtering to obtain reliable estimates of wind stress and wind stress curl. This filtering does not generally affect estimates on large scales, but it effectively eliminates the possibility of investigating the relationship between wind stress and wind stress curl and the ocean response on smaller spatial scales. Initially, the two pixels nearest to the coast (a distance of approximately 50 km) are contaminated, preventing coverage of perhaps the most important zone to wind-driven upwelling. Because of the absence of measurements over the ocean and simplistic estimates of wind stress, detailed maps of coastal wind stress and wind stress curl, arguably the most important forcing factors to the coastal ocean, are still not available (excluding a few limited aircraft measurements). Advances in satellite retrieval techniques, atmospheric modeling, and computational technology, however, allow for new methods of investigating wind stress and its evolution and spatial distribution over the ocean.

We focus on wind stress and wind stress curl for the

Corresponding author address: Dr. Darko Koračin, Desert Research Institute, 2215 Raggio Pkwy., Reno, NV 89512.
E-mail: darko@dri.edu

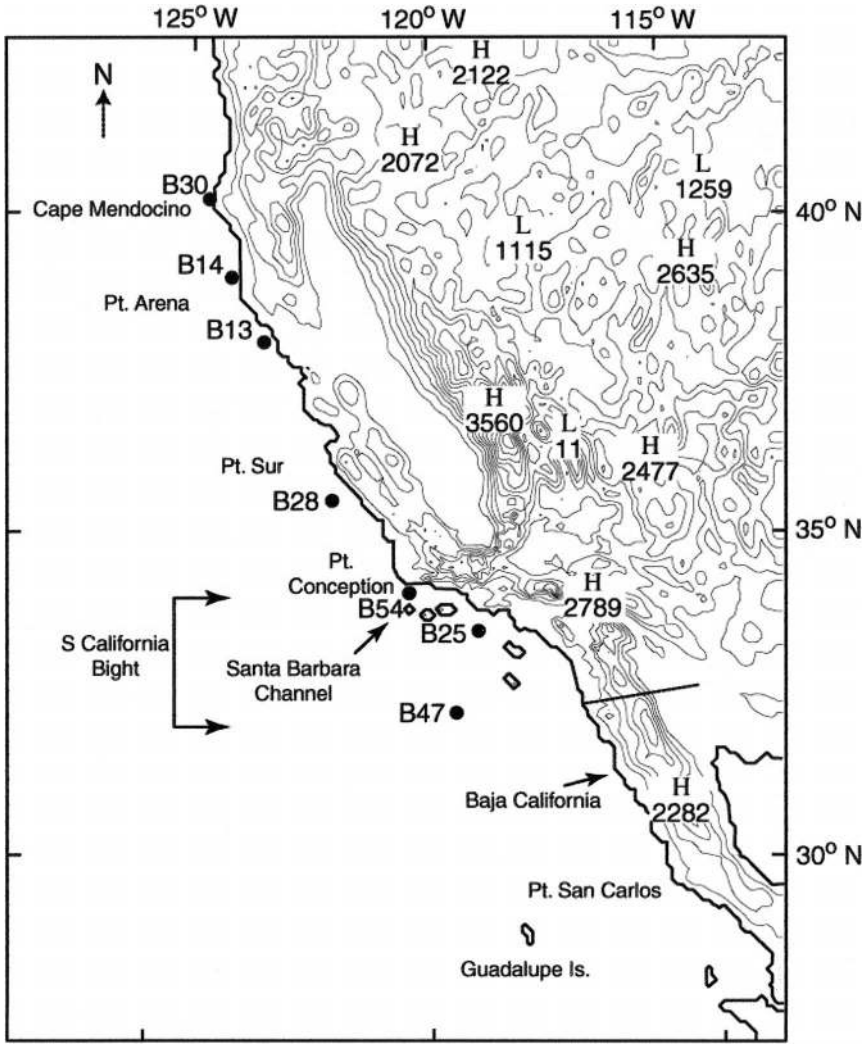

FIG. 1. Map of the MM5 domain and topography with buoy locations and key geographical points. The N–S coastline orientation changes to SE at Cape Mendocino, initiating a California-scale expansion fan with high wind speed and wind stress. The coastline change to E at Point Conception is responsible for the largest positive wind stress curl in the area.

major wind-driven coastal upwelling zone off the coast of California and northern Baja California. The mean summer sea level pressure field is set up by the North Pacific anticyclone off the U.S. West Coast and a thermal low over the southwestern United States. This pressure gradient drives winds to the south along the coast from southern Oregon to central Baja California, as confirmed by ship measurements (Nelson 1977), nearshore buoys and coastal stations (Halliwell and Allen 1987; Dorman and Winant 1995; Dorman et al. 2000), and regional/mesoscale numerical modeling (Dorman et al. 2000; Koračin and Dorman 2001).

A unique element of the California atmospheric marine layer during summer is that it has hydraulic properties with expansion fans in the lees (faster flow and shallower marine layer) and compression bulges on the upwind sides of the capes (slower flow and deeper marine layer), as reviewed in Koračin and Dorman (2001). In addition to cape-scale expansion fans, there is a California-scale expansion fan due to the eastward bend of the California coast (Edwards 2000).

In order to investigate the spatial and temporal structure of wind stress and wind stress curl along the California and northern Baja California coast, we conducted a numerical experiment using the fifth-generation Pennsylvania State University–National Center for Atmospheric Research (NCAR) Mesoscale Model (MM5; Grell et al. 1995). Simulations with 9-km horizontal resolution were performed for all of June 1999 for the region indicated in Fig. 1. We evaluated the model using buoy and satellite data, and the simulated wind fields were used to compute the hourly wind stress by two common algorithms. The simulated wind stress field was used to compute wind stress curl along the California

and Baja California coasts. Our main objective was to investigate spatial and temporal variability of the winds, wind stress, and wind stress curl in response to coastal topographic forcing of the marine airflow. We discuss the mechanisms for generating wind stress and wind stress curl and their effects on coastal upwelling.

2. Model setup

MM5 is a community model that has been developed jointly by NCAR and The Pennsylvania State University (Dudhia 1993; Grell et al. 1995) and has been used worldwide in a variety of research and application studies. Specifically, MM5 has been employed in studies of atmospheric dynamics along the California coast (Koračin and Dorman 2001) and as a driver for an ocean model (Powers and Stoelinga 2000; Beg Paklar et al. 2001). For the purpose of this study, MM5 was run in a nonhydrostatic mode with 9-km horizontal resolution and an integration step of 27 s for all of June 1999. The month of June was selected because significant upwelling along the U.S. West Coast occurs during the late spring and early summer months. The model domain consisted of 149 $\times$ 191 grid points in the horizontal and 35 sigma levels in the vertical direction. The model domain was represented as a Lambert conformal map projection and was centered at 35.15°N, 120.65°W. Topography was read from the 30″-resolution global terrain and land use files. First-guess synoptic fields for every 12 h were obtained from the National Centers for Environmental Prediction (NCEP) Global Data Assimilation System archive. Synoptic information includes virtual temperature, geopotential height, *U* and *V* wind components, and relative humidity on a global grid with a horizontal resolution of 2.5° in both latitudinal and longitudinal extensions. This synoptic information was horizontally interpolated onto the model grid by a two-dimensional, 16-point overlapping parabolic fit. Assimilation of all available upper-air and surface station data into the synoptic fields was performed by objective analysis using a model grid extended horizontally by 180 km on all sides. Twelve-hour lateral boundary conditions (from NCEP reanalysis fields) were used to run MM5 for the entire period. Model options include mixed phase microphysics, parameterization of shortwave and longwave radiation including cloud–radiation effects, and the Grell cumulus parameterization (Grell et al. 1995). Surface heat and moisture fluxes were computed, and the surface temperature was predicted using a surface energy balance algorithm and a five-layer soil model. The Gayno–Seaman turbulence parameterization (Shafran et al. 2000) was chosen, which provides the turbulence kinetic energy as a prognostic variable based on level-2.5 turbulence closure (Mellor and Yamada 1974). Figure 1 shows the model grid setup with topography and geographical locations that will be referenced in the text.

3. Model evaluation

MM5 has been evaluated for many applications (see information online at http://www.mmm.ucar.edu/mm5) and appears to be a reliable modeling tool in atmospheric studies. It is still important, however, to evaluate the model results in predicting complex coastal dynamics. Koračin and Dorman (2001) used MM5 to simulate wind and wind divergence fields along the California coast for all of June 1996 and evaluated the modeled winds using data from the National Data Buoy Center (NDBC) and coastal wind profilers with more than 18 000 comparison points. Koračin and Dorman (2001) also used satellite visual cloud image and infrared data to indirectly evaluate the wind divergence field near the coast and offshore. Their study shows that MM5 is a sufficiently accurate tool to predict the main characteristics of the marine-layer dynamics along the U.S. West Coast.

In this paper, we examine the accuracy of MM5 in predicting the marine atmospheric boundary layer dynamics for all of June 1999 using NDBC buoys as a reference. The accuracy of buoy-measured winds has been established for northern California NDBC buoys during summer (Friehe et al. 1984) and winter (Beardsley et al. 1997) by aircraft flying at about 30-m altitude over the buoy. Adjustment to a common height was accomplished with the Large and Pond (1981) bulk parameterization. Agreement was good, with an aircraft minus buoy wind speed average difference and standard deviation of 0.6 $\pm$ 0.8 m s^{-1}. It should be noted that the scatter has been linked to unresolved variables characterizing the ocean wave field, difference between the wind and wave field vectors, and other factors (reviewed in Jones and Toba 2001).

We selected seven buoys representing the northern, central, and southern areas of the California coast and compared data from these sources with model results at corresponding points. Buoy locations are shown in Fig. 1. The main statistics of the comparison are shown in Table 1. The model was able to correctly reproduce the magnitude of the observed wind speed, and modeled results compared to measurements achieved high correlation coefficients ranging from 0.61 to 0.82. In particular, there were four buoys for which the model yielded correlation coefficients greater than 0.8. The weakest correlation of modeled versus observed wind speed was for buoys 46025 and 46030. One possible reason is that simulations of low wind speeds include model uncertainty due to weak forcing of the dynamics (buoy 46025). Generally, model results can smooth extremes as compared to local point measurements (decreasing high and increasing low values). This is mainly due to the influence of neighboring points on a numerical solution for a given point in the presence of significant spatial gradients. Buoy 46030 is located in a complex position near Cape Mendocino, and the present model

TABLE 1. Basic statistics of the MM5 evaluation for wind speed (m s^{-1}) using the buoy data for all of June 1999; *N*: number of observations, ME: mean error-bias, MAE: mean absolute error, rmse: population root-mean-square error, and rmsve: root-mean-square vector error.

Buoy	Location (°N)	Location (°W)	*N*	Mean MM5 (m s^{-1})	Mean obs (m s^{-1})	Std dev MM5 (m s^{-1})	Std dev obs (m s^{-1})	Correlation coef	ME (m s^{-1})	MAE (m s^{-1})	Rmse (m s^{-1})	Rmsve (m s^{-1})
46013	38.20	123.30	671	8.87	9.10	2.55	3.91	0.82	0.23	1.82	2.34	2.97
46014	39.20	124.00	671	7.96	7.96	2.92	3.67	0.71	0.00	1.94	2.55	3.26
46025	33.70	119.10	671	4.10	3.25	2.29	2.01	0.67	0.85	1.53	1.97	1.97
46028	35.74	121.89	671	7.38	8.91	2.26	3.93	0.81	−1.53	2.53	2.92	3.39
46030	40.42	124.53	672	7.30	6.93	2.39	1.87	0.63	0.37	1.59	1.93	8.67
46047	32.43	119.53	671	6.41	7.85	2.31	2.57	0.82	1.44	1.76	2.06	2.26

resolution is not sufficient to resolve details of coastal topographic effects at that location.

As an illustration of the model evaluation, comparisons between simulations and measurements at a high wind regime location (buoy 46013) and a low wind regime location (buoy 46025) are shown in Fig. 2. A time series of wind speed and wind direction shows that MM5 was able to correctly reproduce wind speed patterns with three periods of increased winds, three short-term wind minima, and persistent wind direction throughout the entire month (buoy 46013; Fig. 2a). Some of the differences between the model simulations and measurements can be attributed to differences in sampling—buoy data is an 8-min average at every hour, while model results represent grid- and time-averaged values. The model correctly reproduced the range of low wind speeds as well as significant wind speed and direction variations at buoy 46025 (Fig. 2b). Table 1 also shows that the bias between modeled and observed wind speed is significantly smaller than the standard deviations of both the modeled and observed time series of wind speed.

An additional method of evaluating model results is to perform spectral analysis of a wind speed time series. Power spectra for model simulations and measurement results at the location of buoy 46013 are shown in Fig. 3. In both cases, the model simulations showed similar spectral behavior to measurements but overestimated the influence of diurnal oscillations as compared with oscillations for shorter periods. Model simulations and measurements both showed significant diurnal peaks at both locations, increased spectra in the inertial oscillation range, and semidiurnal peaks.

Since the number of operational meteorological buoys is few, they provide limited information on the spatial structure of winds over the ocean. In recent years, satellite-based, microwave observations are emerging as an excellent source of information on surface winds over the open ocean. The satellite-borne Special Sensor Microwave Imager (SSM/I) was the most advanced system available in June 1999; it provided wind speed but not direction. Wentz (1997) used NDBC and other meteorological buoys to find that for wind speeds, the systematic error for SSM/I is 0.3 m s^{-1} and the rms error is 0.9 m s^{-1}. In the coastal ocean, SSM/I satellite winds are contaminated and unusable if closer than two pixels to land, which includes most of the NDBC buoys along coastal California and Oregon. Away from land, there remains active discussion about satellite-based accuracy because of the lack of an appropriate measurement system. The only long-term ground truth measurements are provided by buoys, single point measurements that are not related in a simple way to satellite measurements over an area with a 25-km footprint (Larsen et al. 2001). Special care should be exercised when comparing buoys along the western coast of the United States with satellite data since most of the buoys are located 15–25 km from the coast. Taking the nearest offshore pixel is unrepresentative of an inshore buoy (we will show later that this is the most intense field of wind, wind stress, and wind stress curl). The reactivated NDBC buoy 46047, however, is sufficiently far offshore to be compared with uncontaminated satellite wind measurements. This allows intercomparison of buoy, satellite, and model simulations for June 1999. During this time, there were twice-a-day passes near 0800 and 2000 LST, but track gaps reduced these to 37 satellite measurements for the month. The wind speed mean and standard deviation for the buoy 46047 data, MM5 results, and the satellite measurements are shown in Table 2. Correlation coefficients among buoy data, model grid-averaged results, and satellite area-averaged data are very high and are similar, ranging from 0.73 to 0.82. Both MM5 and the satellite underestimate buoy measurements; however, the bias for model versus buoy and satellite versus buoy data is small in comparison with any of the standard deviations (buoy, model, and satellite). A time series (Fig. 4) of all three results confirms that they track each other fairly well except for an occasional deviation. Both the satellite and MM5 results reproduced the major strong-wind events during 3–4, 7–16, 19–22, and 25–27 June as well as minima around 5, 18, 23–24, and 28–29 June.

In order to evaluate simulated winds over the ocean, we compared SSM/I satellite-derived and simulated surface wind speed averaged for all of June 1999 (Fig. 5). The simulated wind speed field agrees reasonably well with satellite-derived winds, although there are significant differences in sampling and averaging procedures, spatial resolution (0.25° for satellite and 9 km for the model), and height representativeness, and there are limitations of satellite detection near the coast. Both the

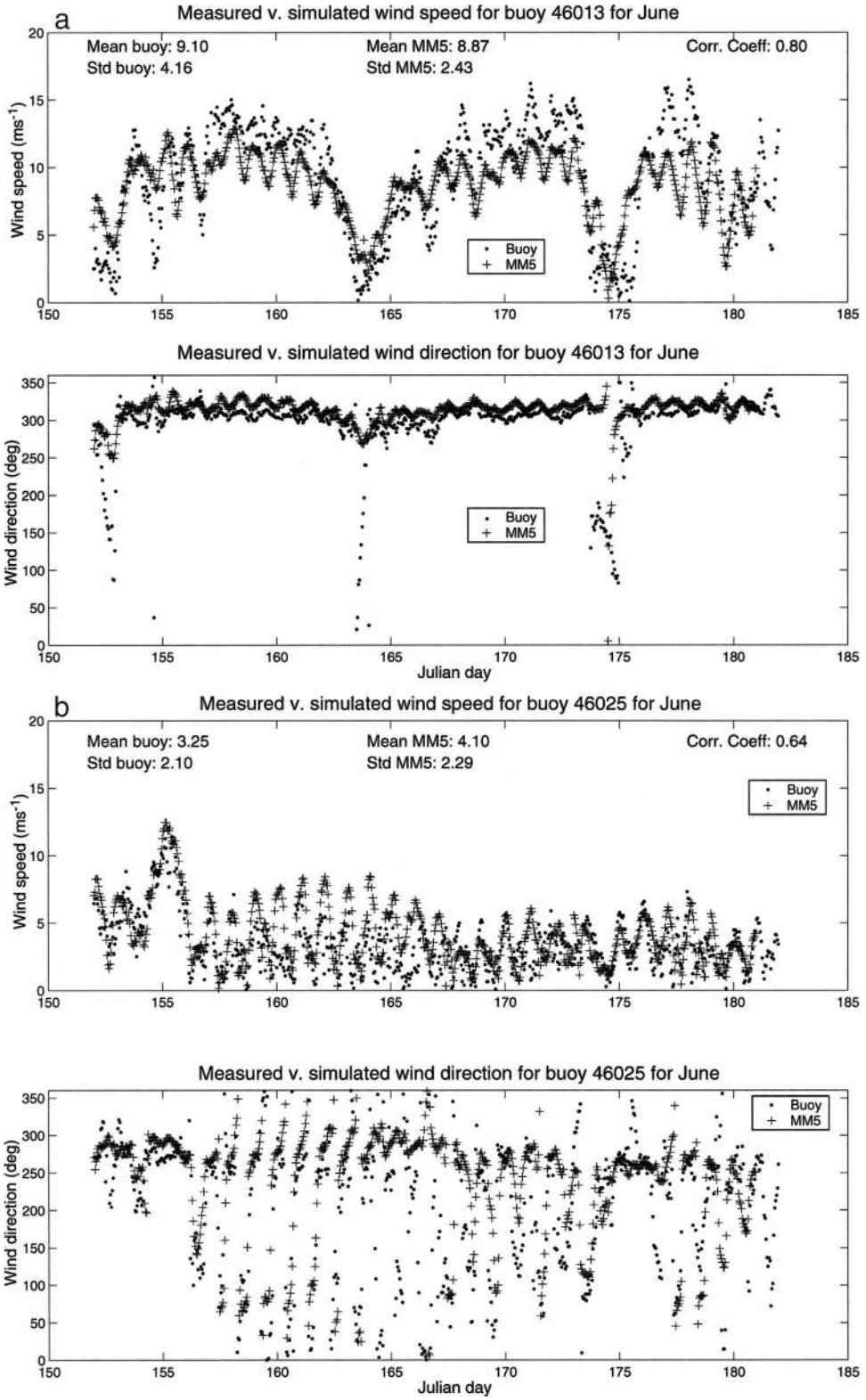

FIG. 2. Time series of hourly surface wind speed and direction as measured (dots) and simulated (plus signs) at (a) buoy 46013 and (b) buoy 46025 for all of Jun 1999.

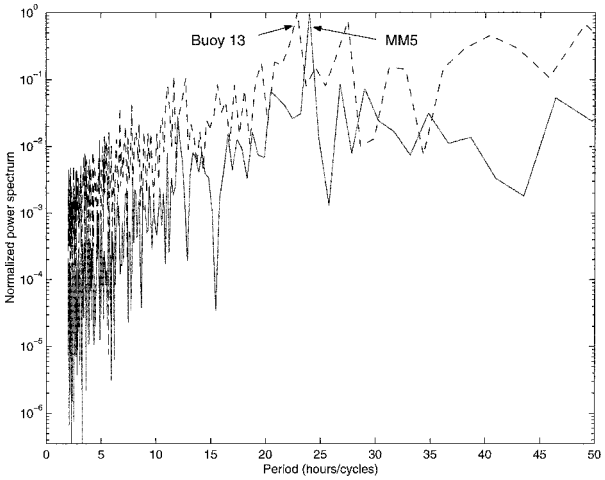

FIG. 3. Normalized power spectra computed from buoy 46013 data (dashed line) and MM5 results (solid line) for all of Jun 1999. Model and buoy show similar diurnal oscillations. Arrows point to diurnal peaks.

SSM/I measurements and simulations clearly agree on a broad high-speed wind zone along northern and central California with maxima centered in the lee of Point Arena. The satellite-derived field also confirms that major capes (e.g., Cape Mendocino, Point Arena) induce persistent flow disturbances in terms of significant wind speed maxima in their lees. The modeled large area of low wind speed on the eastern side of the California Bight and farther southward also can be seen in the satellite data.

4. Marine-layer winds

Figure 6 shows surface wind vectors simulated with MM5 and averaged for all of June 1999. The model results show adjustment of northerly offshore flows into dominantly northwesterly flows near the coast with wind speed generally increasing toward the coast. The average flow structure for June 1999 appears to be similar to the average flow for June 1996 (Koračin and Dorman 2001). A noticeable sequence of expansion fans and deceleration areas is present with the simulated monthly mean average wind speed up to 8.8 m s^{-1} in the lees of major capes. In most of the lees, the wind maximum is confined in a laterally narrow offshore band with a width of about 100 km or less. Near Point Conception, the area of maximum wind is elongated about 200 km in the offshore direction due to the sharp turn of the coastline and the effects of islands on the flow. Considering a broader view, Figs. 5 and 6 suggest that the northern and central California coasts represent a regional (California)-scale lee, an interpretation supported by a numerical model study (Edwards 2000) and an observational study (Edwards et al. 2001). Here, the California-scale expansion fan is marked by the enhanced wind speed area bordered by the 6.5 m s^{-1} wind

TABLE 2. Comparisons among MM5 simulation, satellite SSM/I, and NDBC buoy 46047 wind for the 33 time intervals common to all three during Jun 1999.

	Mean (m s^{-1})	Median (m s^{-1})	Std dev (m s^{-1})	Correlation coef	
				With buoy	With satellite
Model	6.50	6.74	2.48	0.73	0.76
Satellite	6.79	6.60	2.58	0.82	
Buoy	7.76	8.40	2.71		0.82

speed isotach (Fig. 6). This appears to be a significant, persistent feature found in ship observations (Nelson 1977), buoy and coastal stations (Dorman and Winant 1995; Dorman et al. 2000), and MM5 simulations for all of June 1996 (Koračin and Dorman 2001). The southeastern portion of the Southern California Bight is a weak wind zone with a substantial cross-shore, nonupwelling-favorable wind direction. The upwelling-consistent, shore-parallel flow along southern California is reestablished near 33°N and continues along northern Baja California. Wind speed variability during June 1999 is represented by its standard deviation (Fig. 7). Most of the flow variability appears to be in the narrow zone near the coast. The 2 m s^{-1} isoline roughly marks the area of the California regional-scale lee, while the 2.5 m s^{-1} and greater isolines indicate coastal mesoscale flow forcing by topographic features. One of the two areas with the greatest standard deviation is in the lee of Cape Mendocino, which may be due to this area being on a fluctuating edge of the northern end of the California-scale high wind speed region (Dorman et al. 2000; Haack et al. 2001). The lee of Point Arena does not have a peak variation as it is more solidly in the center of the persistent high speed winds. The other extreme variability area is in the immediate lee of Point Conception with its right angle coastal bend, the island

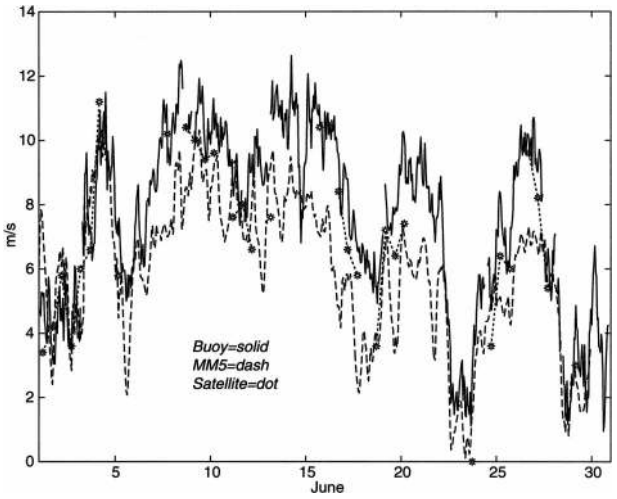

FIG. 4. Time series of wind speed for buoy 46047 data (solid line), MM5 results (dotted line), and SSM/I satellite data (dashed line with stars) for all of Jun 1999.

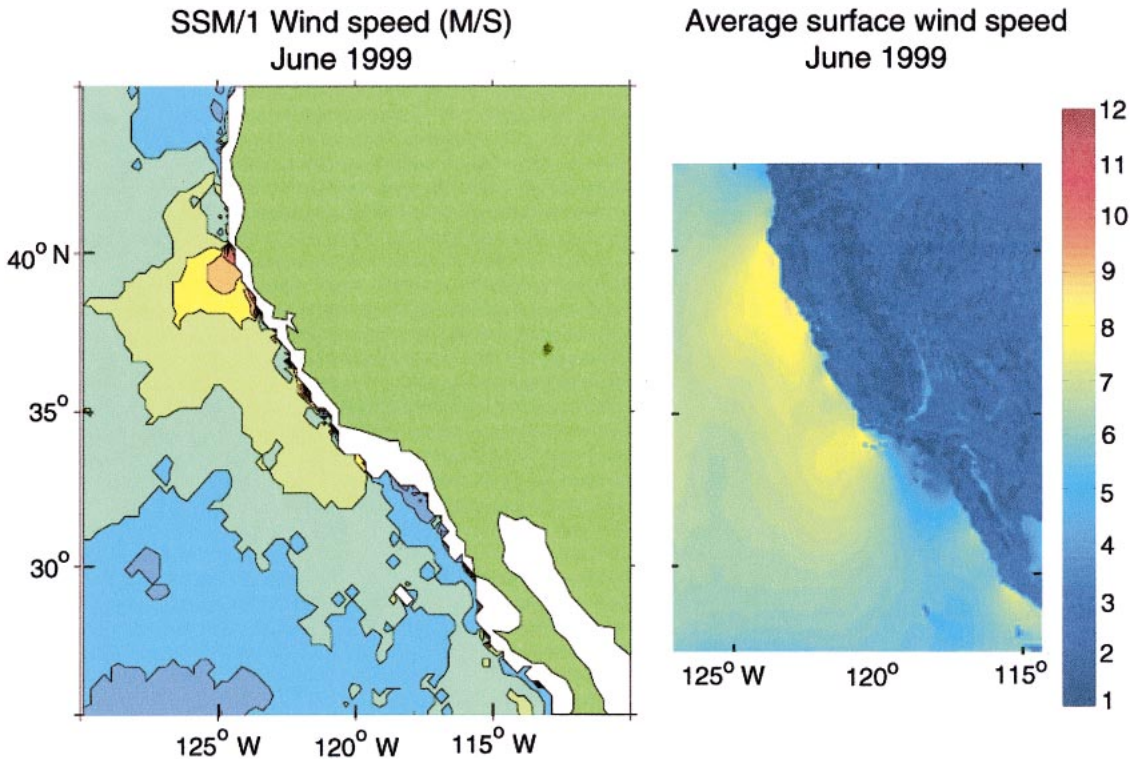

FIG. 5. Surface wind speed (m s^{-1}) averaged for all of Jun 1999 as (left) derived from SSM/I satellite data and (right) simulated with MM5.

lees, and weak winds in the eastern portion of the Southern California Bight. Secondary maxima are in the Monterey and Point Sur regions. The figure also shows that the islands in the Southern California Bight and off the Baja California coast significantly modify the flow creating narrow lees many times longer than the islands themselves.

5. Wind stress

The temporal and spatial structure of wind stress is crucial to understanding the forcing of the ocean current and coastal upwelling. We investigate the stress by comparing two algorithms for estimating bulk wind stress over the ocean, namely, those according to Large and Pond (1981) and Deacon and Webb (1962). These two algorithms, hereinafter denoted as LP and DW, are used to examine whether different formulations will induce significant differences in the pattern of the wind stress and wind stress curl. A number of algorithms for wind stress computation, starting with the early work by Rossby and Montgomery (1935), are discussed by Toba et al. (2001). According to Toba et al. (2001), the Large and Pond (1981) algorithm is based on one of the largest measurement datasets. Beardsley et al. (1997) showed that some more recent algorithms, such as the Tropical Ocean and Global Atmosphere Coupled Ocean–Atmosphere Research Experiment (TOGA COARE; Fairall et al. 1996), produce essentially the same results as the Large and Pond algorithm. The Large and Pond algorithm has been commonly used in atmospheric and oceanic studies (e.g., Dorman and Winant 1995; Wentz 1997; Dorman et al. 2000; Samelson 2002). The Deacon and Webb algorithm was chosen in our study as one of the possible upper limits of estimated stress because it has one of the greatest intercept parameters (1.0) and a significant coefficient (0.07) in the relationship between drag coefficient and wind velocity [see below and also Toba et al. (2001)]. In the first step of our analysis, we used simple expressions empirically determined for near-neutral stability conditions. The assumption of near-neutral conditions in June for the simulated area is supported by ship observations, which show that the majority of the bulk Richardson stability index offset from the neutral induces a change in wind stress in the range of −4% to +1% (Nelson 1977). According to the LP algorithm, bulk stress τ_{LP} is calculated as follows:

$$\tau_{\mathrm{LP}} = \sqrt{(\tau_{x,\mathrm{LP}})^2 + (\tau_{y,\mathrm{LP}})^2}, \qquad \tau_{x,\mathrm{LP}} = \rho C_{d,\mathrm{LP}} \overline{V} U,$$

$$\tau_{y,\mathrm{LP}} = \rho C_{d,\mathrm{LP}} \overline{V} V, \qquad \overline{V} = \sqrt{U^2 + V^2}, \quad \text{and}$$

$$C_{d,\mathrm{LP}} = \begin{cases} 1.2 \times 10^{-3} & \text{for } 4 \le \overline{V} < 11 \text{ m s}^{-1} \\ (0.49 + 0.065\overline{V}) \times 10^{-3} & \text{for } 11 \le \overline{V} \le 25 \text{ m s}^{-1}, \end{cases} \quad (1)$$

where U and V are wind components in the X and Y

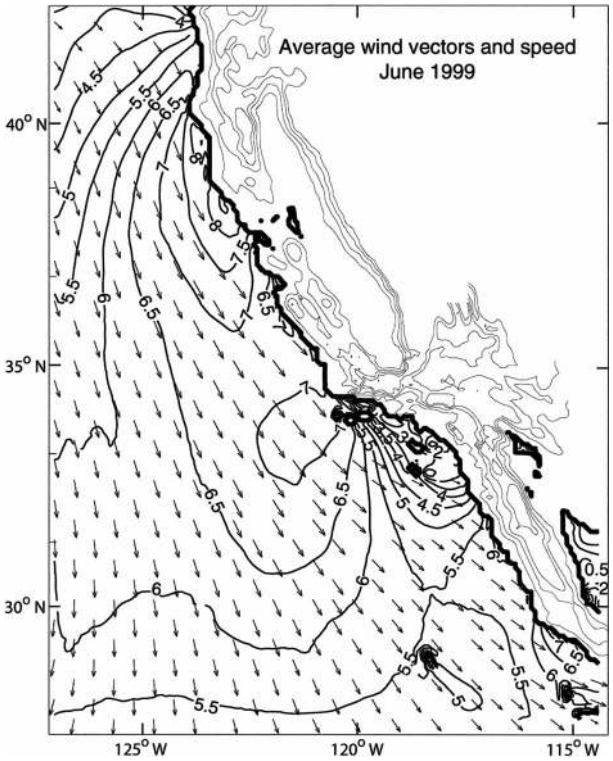

FIG. 6. Simulated wind vectors and contours of surface wind speed (m s^{-1}) averaged for all of Jun 1999. Contour interval is 0.5 m s^{-1}. Expansion fans form high-speed areas on the California scale (enclosed by 6.5 m s^{-1}) and in the lees of every major cape.

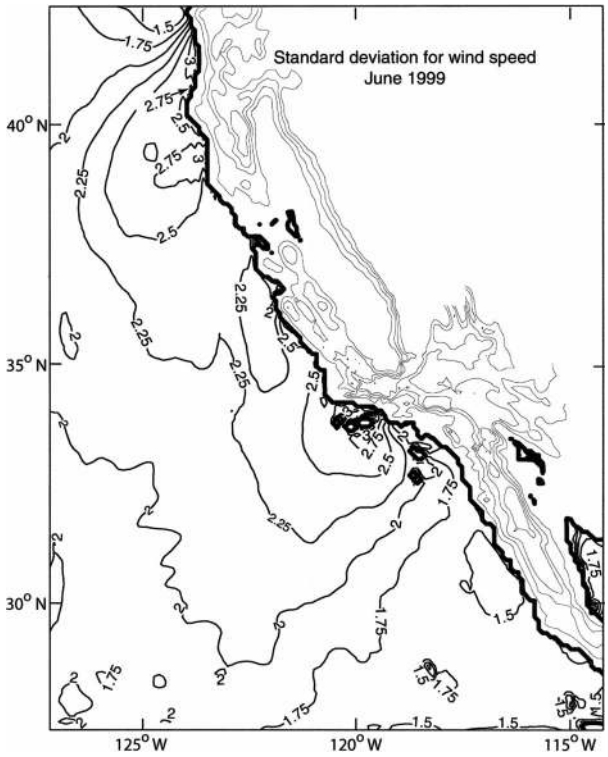

FIG. 7. Standard deviation of the simulated surface wind speed (m s^{-1}) as determined from MM5 simulations for all of Jun 1999. Contour interval is 0.25 m s^{-1}. Maxima are in the lees of major capes. The 2.25 m s^{-1} isoline is coincident with the California-scale expansion fan.

directions, respectively; ρ is the air density; C_d is the drag coefficient for neutral conditions; $\overline{V}$ is the resultant wind speed; and the subscript LP refers to the Large and Pond algorithm.

According to the DW algorithm, bulk stress τ_{DW} is calculated as follows:

$$\tau_{DW} = \sqrt{(\tau_{x,DW})^2 + (\tau_{y,DW})^2}, \qquad \tau_{x,DW} = \rho c_{d,DW} \overline{V} U,$$
$$\tau_{y,DW} = \rho c_{d,DW} \overline{V} V, \qquad \overline{V} = \sqrt{U^2 + V^2}, \quad \text{and}$$
$$C_{d,DW} = (1 + 0.07\overline{V}) \times 10^{-3}, \tag{2}$$

where the notation is the same as above except that the subscript DW refers to the Deacon and Webb algorithm. Both algorithms are developed for wind speed at 10 m and near-neutral atmospheric stability conditions in the surface atmospheric boundary layer.

Figure 8 shows simulated wind stress averaged for all of June 1999 using algorithms by LP and DW. The general patterns of the simulated wind stress are similar for both schemes. The greatest stress is coincident with the strongest winds, which are offshore of Cape Mendocino and Point Arena with secondary maxima southwest of Point Conception, off Point Sur, and off the northern Baja California coast. A large area of low wind stress extends from the eastern side of the Southern California Bight southward through San Diego coastal waters. Significantly low values are simulated in the lees of islands in the Southern California Bight and off the southern California coast. The area of the California regional-scale lee that was seen in the simulated winds is also seen in the wind stress and is bordered by the 0.07–0.08-Pa wind stress isoline (LP algorithm). When using these algorithms, we found that wind stress is greater when using the DW scheme compared to using the LP algorithm; however, the main features are similarly captured by both schemes. Maximum wind stress from all hourly simulations in June 1999 up to 0.37 Pa (LP) and 0.52 Pa (DW) is confined to the nearshore zone of about 50 km where maximum winds are predicted. Similar to the locations of the highest monthly averaged values, the main maxima are in the lees of Cape Mendocino, Point Arena, Point Sur, and near Point Conception. A plot of the standard deviation of wind stress (not shown) confirms that the greatest monthly stress variability is in the California regional-scale lee. The strength of this expansion fan is significantly dependent on the alignment of the synoptic flow with respect to the coastline and coastal topography.

We compared wind stress estimates for the LP and DW algorithms using buoy data and model results at corresponding buoy locations. Since the simulated winds showed high correlation with measurements but generally underpredicted some of the high wind mea-

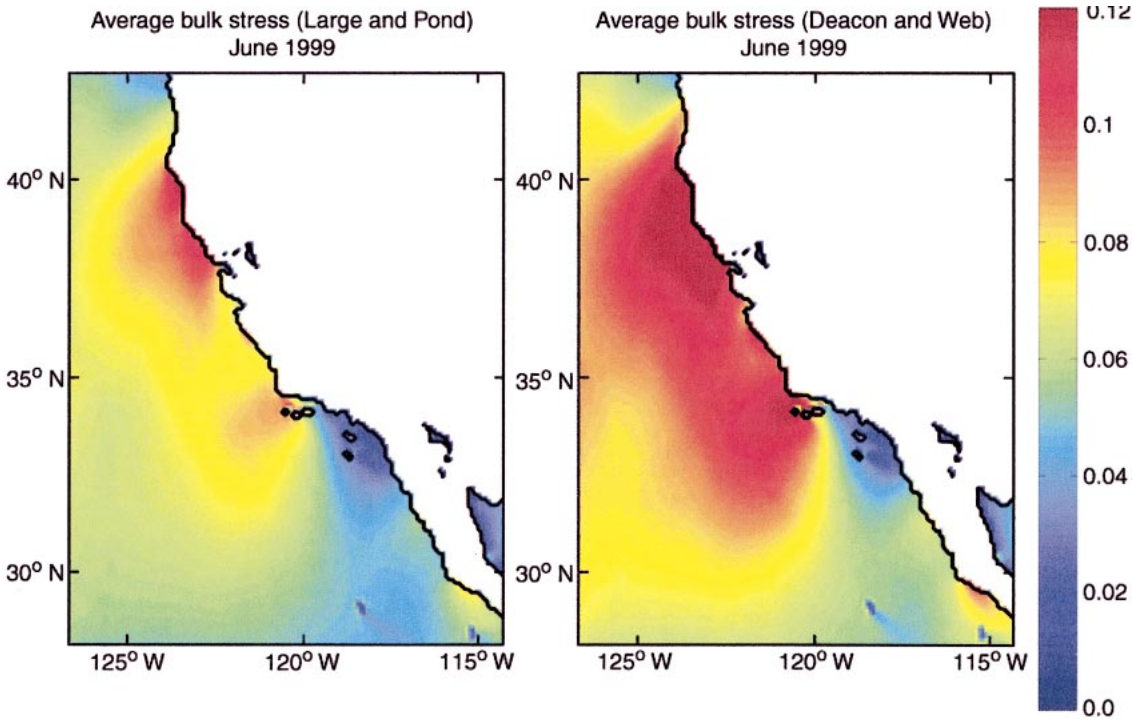

FIG. 8. Averaged wind stress (Pa) for all of Jun 1999 calculated using the (left) Large and Pond and (right) Deacon and Webb algorithms. Largest stress is found near the coast, and extreme values are found in expansion fans in the lees of capes. The patterns and extreme-value center locations are independent of the wind stress algorithm.

surements (Table 1), the wind stress calculated from the model results in these cases also underpredicted the buoy-estimated wind stress. Although the simulated wind stress underestimates most of the higher peaks of the stress computed from buoy data, it is of the same order of magnitude, closely follows the time evolution of the observed stress, and correlates well with the stress estimated from the buoy data (Fig. 9). It should be mentioned that the model, because of its spatial and temporal averaging, cannot reproduce the sharp wind peaks measured by the buoy as an 8-min average every hour. Buoy 46030 is located at the edge of the upwind side of Cape Mendocino, and consequently both measurements and model results show relatively small to medium wind stress in comparison with that calculated for other locations. Moving downcost, buoys 46014 and 46013 (Fig. 9) are located in the lees of Cape Mendocino and Point Arena and show intense wind stress throughout

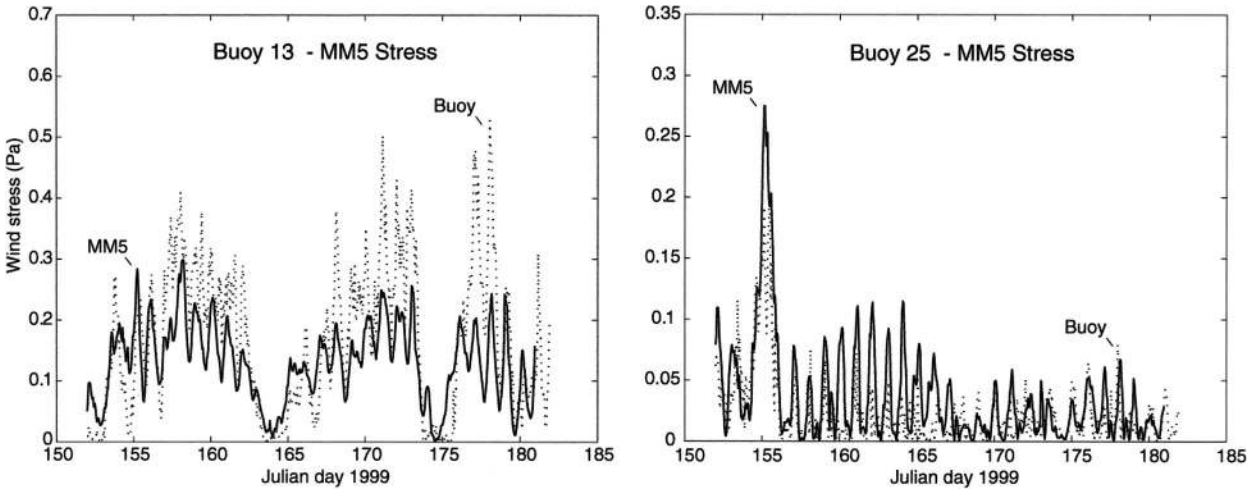

FIG. 9. Time series of wind stress (Pa) as estimated from MM5 (solid line) and buoys (dotted line) at two buoy locations, (left) 46013 and (right) 46025, using the Large and Pond algorithm. Buoy locations are shown in Fig. 1.

the entire month. Buoy 46028 is located in the narrow expansion fan in the lee of Point Sur and also exhibits significant wind stress. According to the measurements, the largest wind stress is estimated at the buoy 46054 location in the immediate lee of Point Conception. The eastern side of the Southern California Bight where buoy 46025 is located is characterized by significant wind minima (Figs. 5 and 6) and wind stress minima (Fig. 9). Consequently, the estimated stress from both measurements and model results in this area is significantly small. Buoy 46047 is located at the downwind edge of the Point Conception expansion fan, and the estimated wind stress is significantly greater than at buoy 46025 but still correspondingly smaller compared to the maximum wind stress at buoy 46054. Since modeled wind stress bias is relatively similar for all buoys and wind direction is captured well by the model (Fig. 2), modeled wind stress can be used to estimate wind stress curl, which cannot be estimated from the sparse and inadequate buoy network.

As a comparison, the ship-based, long-term mean for the June maximum value off northern California (Nelson 1977) is similar to the MM5 June 1999 simulation (about 0.1–0.15 Pa). Ship-based stress is much smoother and broader, however, with areas greater than 0.1 Pa extending farther offshore (400 km) and along the coast (32°–41°N). The MM5 stress value greater than 0.1 Pa extends from 37° to 41°N with the peak value at the coast. It is possible that the inshore minimum of the ship-based stress along northern and central California is due to the avoidance of high wind speed areas that were confirmed by aircraft and buoy measurements cited earlier. It should be mentioned that ship-based stress was computed from available ship observations in squares of 1° on the side.

6. Wind stress curl

The temporal and spatial structures of wind stress curl may play a significant role in oceanic upwelling. Furthermore, the role of wind stress curl in coastal upwelling is poorly understood because of a lack of suitable measurements and computational difficulties. To better understand this role, we used the wind stress results discussed in the previous section to compute the wind stress curl.

Wind stress curl (C) was calculated as

$$C = \frac{\Delta\tau_y}{\Delta x} - \frac{\Delta\tau_x}{\Delta y}, \tag{3}$$

where Δx and Δy are the model grid resolutions in the X and Y directions. Because of the horizontal resolution of 9 km, we are neglecting the earth's curvature effects in the computation of wind stress curl. The average wind stress curl calculated using the LP and DW algorithms for all of June 1999 is shown in Fig. 10a. According to the simulations, a significantly large positive wind stress curl is confined to a narrow band at the coastline while the remainder of the area is dominated by weakly negative wind stress curl.

As the greatest values and gradients of wind stress curl are near the coastline, the subdomain areas of Fig. 10a are shown in Figs. 10b and 10c for easier viewing. The Point Conception and vicinity areas are shown in Fig. 10b. Large positive values of wind stress curl are in the Santa Barbara Channel and island lees, while negative values are found on the north sides of the islands (panel A). On the upwind side of Point Conception, strong positive curl is confined to a narrow coastal band, while the rest of the offshore area is characterized by weak near-zero and negative wind stress curl (panel B). Islands in the eastern part of the Southern California Bight induce long downwind banners of weak positive wind stress curl (panel C). Although the dimensions of the islands are small as compared with the model resolution, they appear to be sufficiently resolved (see Fig. 10b) and induce significant modification of the wind structure and consequent wind stress and wind stress curl. In a subsequent study, we will focus on the Point Conception area using higher horizontal model resolution. Details of wind stress curl in the Cape Mendocino area are shown in Fig. 10c.

In order to understand the spatial structure of the wind stress curl, we considered the basic aspects of the wind stress structure near the coast. Figure 11a shows idealized conditions of the lateral shear of the wind speed that can be expected near coast in the case of weak forcing of the flow by coastal topography when the coastline is parallel to the flow. In this conventional view, wind speed decreases with the decrease in lateral distance toward the coast. Assuming that wind stress is collinear with wind, this would create a positive wind stress curl in that region. In contrast to this conventional picture, present simulations show quite a different flow structure (depicted in Fig. 11b). Wind stress in the expansion fans increases laterally in the direction toward the coastline. Only at the closest distance does the wind stress drop off. This creates a very narrow band of positive wind stress curl in the vicinity of the coastline and a much broader region of negative wind stress curl on the western side of expansion fans. The effect of the nearshore wind maximum (Fig. 11b) resembles the case of wind, wind stress, and curl of wind stress in the lee of Cape Mendocino (see Figs. 5, 8, and 10a,c).

Gradients of the components of wind stress can be used to understand the resultant structure of the wind stress curl (Fig. 12). Let us consider the areas east and west of the maximum stress location near the coast in the lee of Cape Mendocino. In the eastern area (inshore direction), the first term ($\Delta\tau_y/\Delta x$) gives a positive contribution to the curl [Eq. (3)] since the negative values of τ_y are become smaller in absolute magnitude in the X direction. The second term applied to this area ($-\Delta\tau_x/\Delta y$) gives a smaller contribution—weaker gradients as compared with the gradients of the first term—but is, as a whole, a negative contribution since the positive

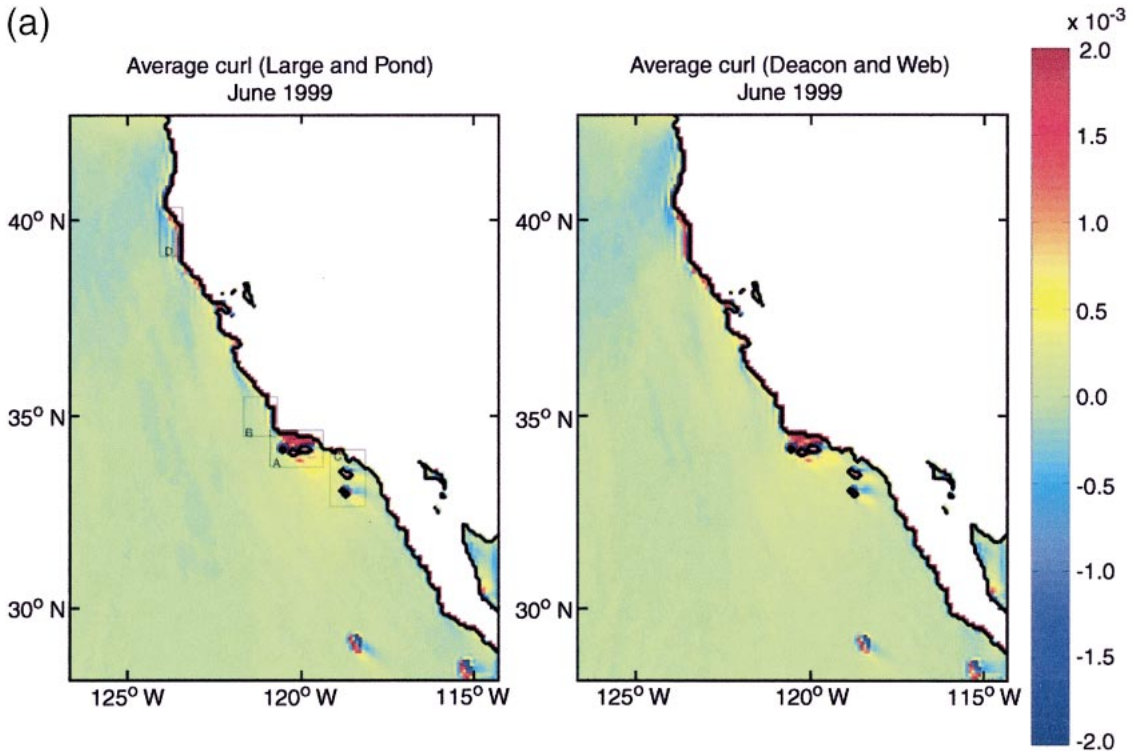

FIG. 10. (a) Average wind stress curl (Pa km^{-1}) for all of Jun 1999 calculated from hourly wind stress curl values estimated with the (left) Large and Pond and (right) Deacon and Webb algorithms. The offshore region is dominated by a weak, positive wind stress curl that is independent of the algorithm. Positive wind stress curl is restricted to the NW portion of the Southern California Bight and close to the coast and islands. Details of the wind stress curl in areas A, B, C, and D are shown in (b) and (c).

values of τ_x are decreasing southward. So, the combined effect of these two curl terms applied to the eastern area (inshore direction) results in a narrow band of positive curl (Figs. 10a,c). In the western area (offshore direction), the first term ($\Delta\tau_y/\Delta x$) gives a negative contribution to the curl [Eq. (3)] since the negative values of τ_y become greater in absolute magnitude in the X direction. The second term applied to this area ($-\Delta\tau_x/\Delta y$) gives small negative or near-zero values since the positive values of τ_x are decreasing southward. So, the combined effect of these two curl terms applied to the western area (offshore direction) is a broad band of negative curl (Figs. 10a,c). The same reasoning can be applied to the Point Arena lee where the positive curl is simulated in a narrow band near the coastline while negative and near-zero curl prevail in the offshore direction. A major turn in the flow occurred downwind of Point Arena where the coastline turns roughly from 360° to 320° alignment. As anticipated by the idealized reasoning (Fig. 11c), the τ_x component increases downwind. As discussed above, this increase induces negative values of the second term in the curl equation and reduces the dominant positive value of the first term in the near-shore zone. Farther downwind, the curvature effect weakens and the gradient of τ_x downwind (second term) becomes negligible. The first term dominates and consequently the curl becomes positive in the offshore direction in a relatively broad band of the San Francisco Bay and Monterey Bay areas.

The two idealized conditions shown in Figs. 11a and 11b considered only variations of the y component of stress in the X direction [see Eq. (3)]. When the coastline bends to the east (Point Arena and Point Conception), there is an additional effect on wind stress curl due to change (downwind increase) in the x component of the stress in the Y direction (Fig. 11c). This results in a significant increase in positive wind stress curl centered to the east of the initial flow band. It should be noted that this effect is due to curving of the flow even when the magnitude of the stress is constant along the flow trajectory. This is further clarified by analyzing the spatial distribution of the surface wind stress components (Fig. 12).

Now, let us consider the reasons for the large positive curl in the lee of Point Conception and the Santa Barbara Channel islands. The largest curl on the eastern side of the lee (Fig. 10b) can be explained as follows. The first term ($\Delta\tau_y/\Delta x$) gives a large positive contribution to the curl [Eq. (3)] since the negative values of τ_y become smaller in absolute magnitude in the X direction. The second term applied to this area ($-\Delta\tau_x/\Delta y$) gives a smaller—weaker gradients as compared with the gra-

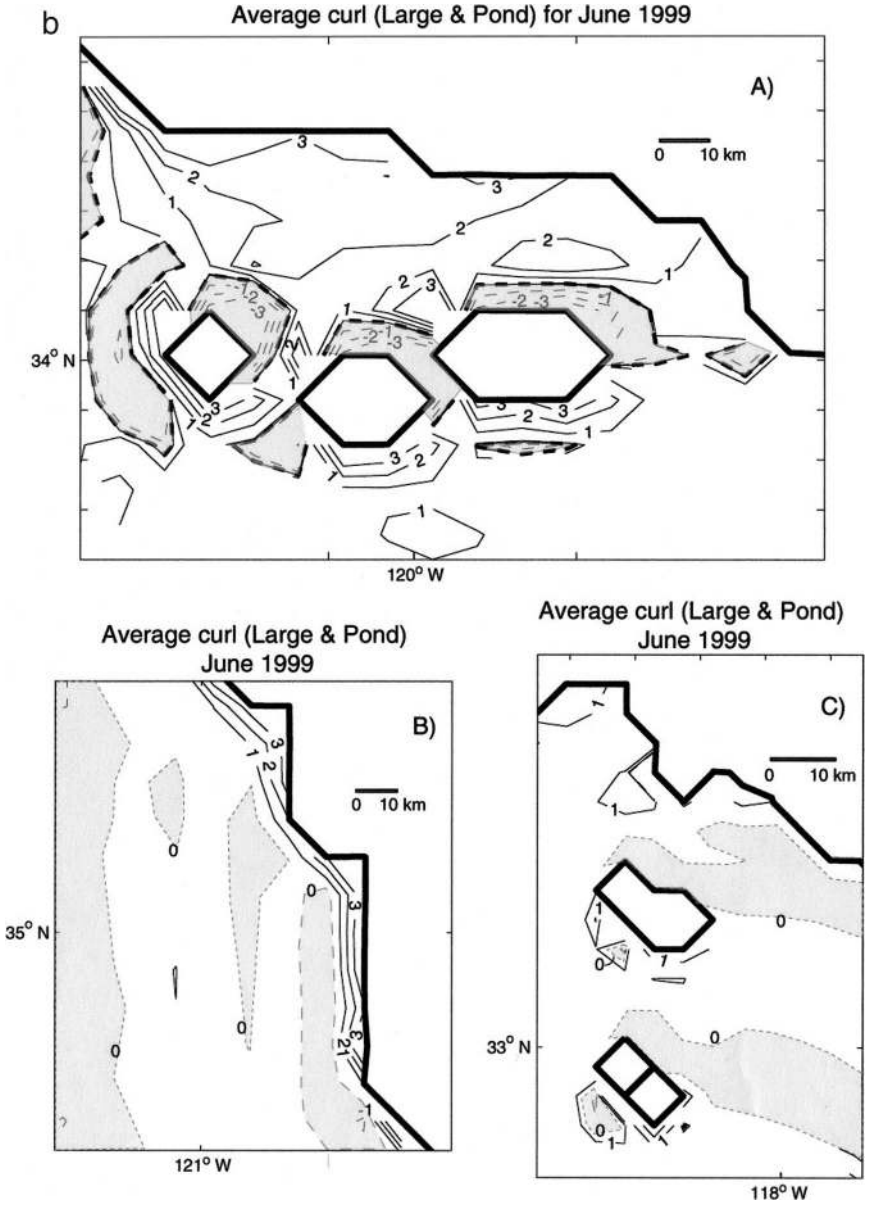

FIG. 10. (*Continued*) (b) Subdomain of (a) showing the monthly average wind stress curl (Pa km^{-1}) for Point Conception areas A, B, and C (using the Large and Pond algorithm). Contour interval is 1×10^{-3} Pa km^{-1} for positive curl values and 0.1×10^{-3} Pa km^{-1} for negative curl values, with an additional contour line with a value of -0.01×10^{-3} Pa km^{-1} to clarify which regions have a low-magnitude negative curl.

dients of the first term—and also positive contribution since the positive values of τ_x increase southward because of the curvature effect (as ideally shown in Fig. 11c). So, the combined effect of these two curl terms applied to the eastern area (inshore direction) results in a significant value of positive curl (Figs. 10a,b). Simulations show that moving westward from that area, the curl is reduced but still positive. The first term ($\Delta\tau_y/\Delta x$) gives a positive contribution to the curl [Eq. (3)] since the negative values of τ_y become smaller in absolute magnitude in the X direction, but the gradients are weaker as compared with the east side of the lee. The second term applied to this area ($-\Delta\tau_x/\Delta y$) gives a small and negative contribution since the positive values of τ_x decrease southward. The combined effect still results in positive curl but of smaller magnitude in comparison with the curl in the eastern area where both terms give positive contributions.

In summary, the model results show that the spatial structure of wind stress curl is a consequence of the nearshore wind stress maximum in conjunction with the downwind variation of coastline alignment. This is the

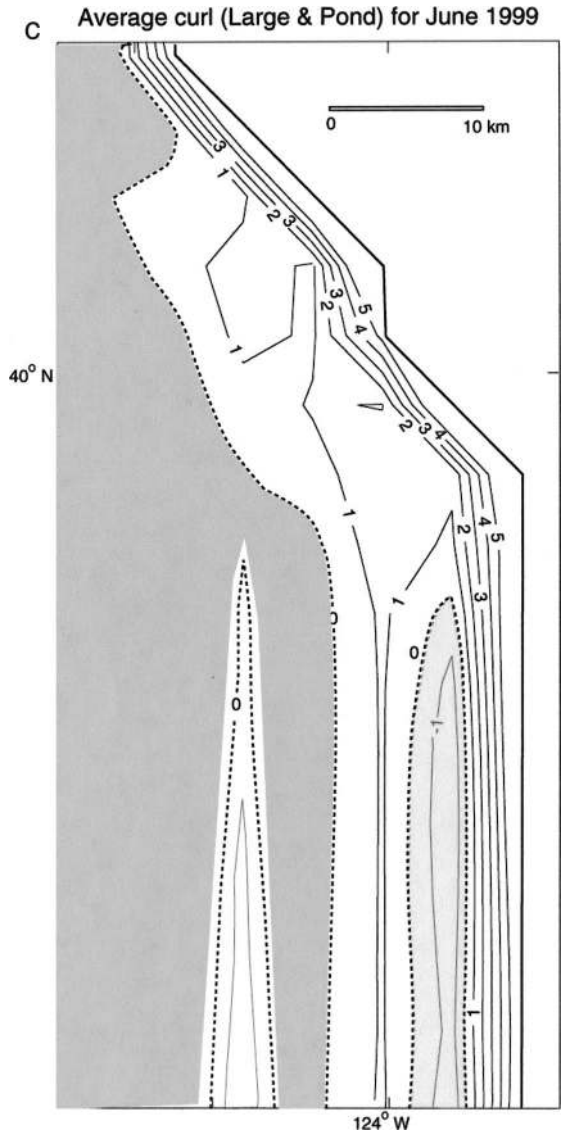

FIG. 10 (*Continued*) (c) Subdomain of (a) showing the monthly average wind stress curl (Pa km^{-1}) for the Cape Mendocino area D in (a) (using the Large and Pond algorithm). Contour interval is 1×10^{-3} Pa km^{-1} for positive curl values and 0.1×10^{-3} Pa km^{-1} for negative curl values, with an additional contour line with a value of -0.01×10^{-3} Pa km^{-1} to clarify which regions have low-magnitude negative curl.

reason for the band of positive wind stress curl that is narrow and near the shore along northern California and broad in the Southern California Bight.

Estimation of possible error in computation of wind stress curl

Since there are no available, spatially dense observations over the ocean, it is not possible to determine model error at points where there are no measurements. For example, we assume that modeled stress has a bias with respect to the stress calculated from buoy data. In this case, that bias is then added to the modeled stress at the neighboring points around the buoy location and the stress calculation will be altered; however, the curl will be the same as before, adding the bias due to the subtraction of the same bias in the *Y* and *X* directions. As an illustration, we consider data for buoy 46013 (Table 1). Applying the average simulated *V* wind component and average wind speed at the buoy location, one can obtain a baseline τ_y. Adding model bias to the average wind speed and the component of the bias in the *Y* direction to the simulated *V*, one can obtain τ_y with bias. In this case, the difference between baseline τ_y and τ_y with bias is 5%. In the other case, if we add 1 m s^{-1} to the wind speed and the appropriate fraction of that value to the *V* wind component [the possible buoy measurement error is up to ± 1 m s^{-1}; Gilhousen (1987)], the difference between this baseline τ_y and the altered τ_y is 25%. So, in this case (and similarly for six out of eight buoys; Table 1), a possible measurement error can induce a greater discrepancy in calculated stress than model bias. Table 1 also shows that all biases are smaller than the standard deviation of the measurements. Error in the computed curl cannot be easily determined; however, using certain assumptions, we can roughly estimate it. Since we do not know the spatial distribution of the bias, we linearly interpolate the bias between two neighboring buoys (46013 and 46014). The change in the wind speed bias is 0.0172 m s^{-1} per each gridpoint separation (9 km). Consider the monthly averaged wind components at the four model points around the buoy 46013 location that are used to calculate wind stress and wind stress curl. First, we compute the wind stress components and wind stress curl (baseline curl). Then we keep the same wind components for the southern and western points, while we add the change in the wind speed bias per two grid separations to the northern and eastern points. Next, we calculate the wind stress components and curl (curl with bias). The difference between baseline curl and curl with bias is 22%. To summarize, bias and error in the wind speed can significantly influence wind stress; however, the computed curl could be altered to a lesser extent. Note also that spatial change of the bias, and not the actual value, is important to determining possible curl error.

7. Synoptic variations of wind, wind stress, and wind stress curl

The purpose of this section is to discuss temporal and spatial variation of sea level winds, wind stress, and wind stress curl in response to midlevel synoptic forcing. Monthly means shown in the foregoing text are averages of individual events that have greatly different wind and wind stress patterns. Edwards (2000) used buoy data and satellite-measured winds to show that the California-scale expansion fan structure and maximum wind speed are related to the synoptic-scale pressure

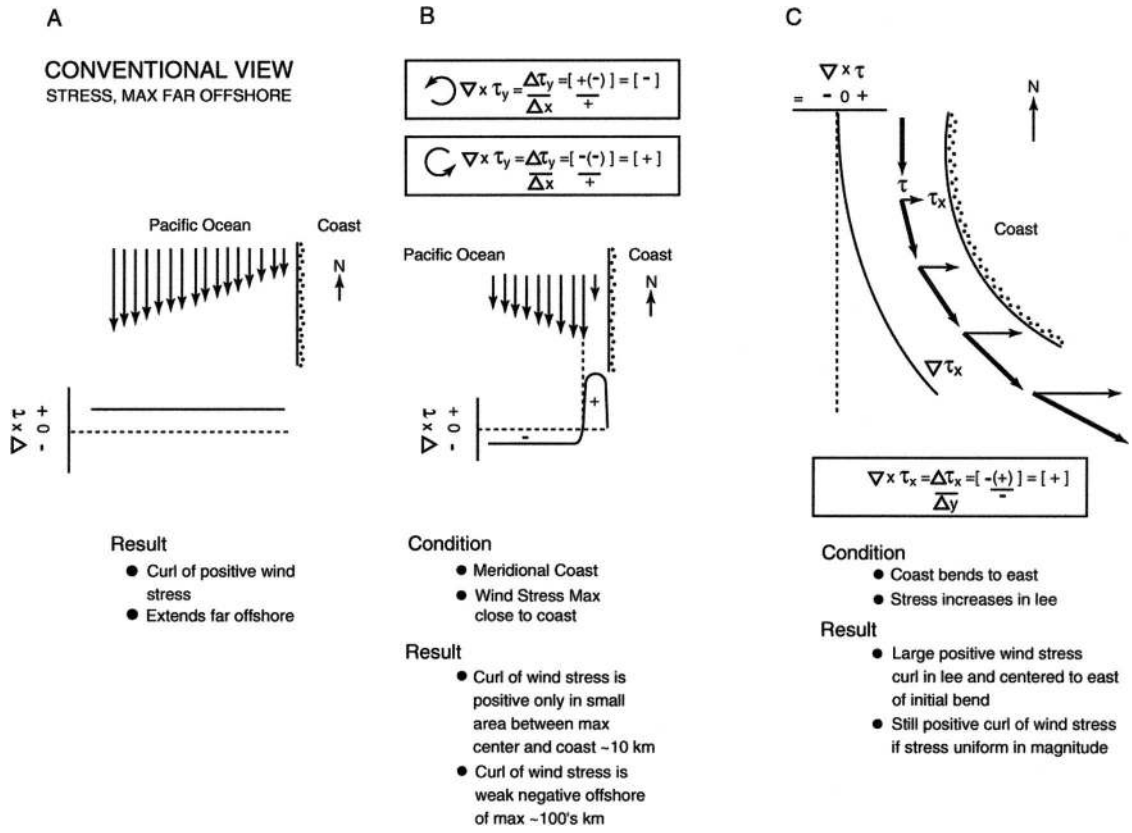

FIG. 11. Schematic of the idealized lateral shear of the surface wind stress in the cases of wind stress maximum (a) far offshore and (b) near shore, and (c) the effect of coastline curvature on the spatial variation of the wind stress and wind stress components. Aircraft, SSM/I satellite, and MM5 simulations corroborate the dominance of the nearshore wind stress maximum for northern and central California. The coastline curvature case applies to the immediate lee of Point Conception.

gradient. Taking a different approach, Cui et al. (1998) applied a numerical model to an idealized California coast and found that the sea level wind field structure is related to the direction of background airflow. Here, we focus on the wind speed and wind stress maxima structure and position along the coast, which provide the strongest signals and are of high interest. Three cases of wind maxima occurring between Cape Mendocino and Point Conception, near Point Conception, and along northern California during June 1999 are shown that are typical of the range of synoptic events.

The first event is a broad, sea level wind speed and wind stress maximum extending from Cape Mendocino to the south of Point Conception on 7 June (Figs. 13a–d). Weak winds and wind stress cover most of the Southern California Bight, with even weaker structure in the island lees. Positive wind stress curl appears along almost the entire California coast in nearshore, narrow bands with peak values in the lees of capes and islands (Fig. 13d). The broad area of high-speed winds is caused by increased pressure gradients associated with a stronger summer 500-hPa trough with a N–S oriented axis crossing the central California coast as reflected in the 500-hPa height (Fig. 14a, bottom row) and temperature (Fig. 14b, bottom row). At sea level, the isobars over the northern and central California coast are nearly meridional with comparatively dense, uniform spacing. The coldest 850-hPa temperatures occur with this event.

The second event has a sea level wind and wind stress maximum around Point Conception extending southward in a narrow band on 15 June (Figs. 13e–h). Weak winds are simulated in the eastern part of the Southern California Bight, Baja California, and the lee of Guadalupe Island as well as around Cape Mendocino. The strongest positive wind stress curl field is in the Santa Barbara Channel and island wakes, while in northern California the nearshore positive curl is weak (Fig. 13h). In this case, there is a WNW–ESE-oriented trough at 500 and 850 hPa west of California extending to 33°N (Figs. 14a,b). The shortest distance to the coast from the trough is at Point Conception, coincident with the sea level wind and wind stress maximum. Thermal gradients are weak at 850 and 500 hPa, causing the strongest sea level pressure gradients to be near central California and Point Conception.

The third event is characterized by a high wind speed and wind stress band that is narrower in comparison with previous events with maxima in the lees of Point

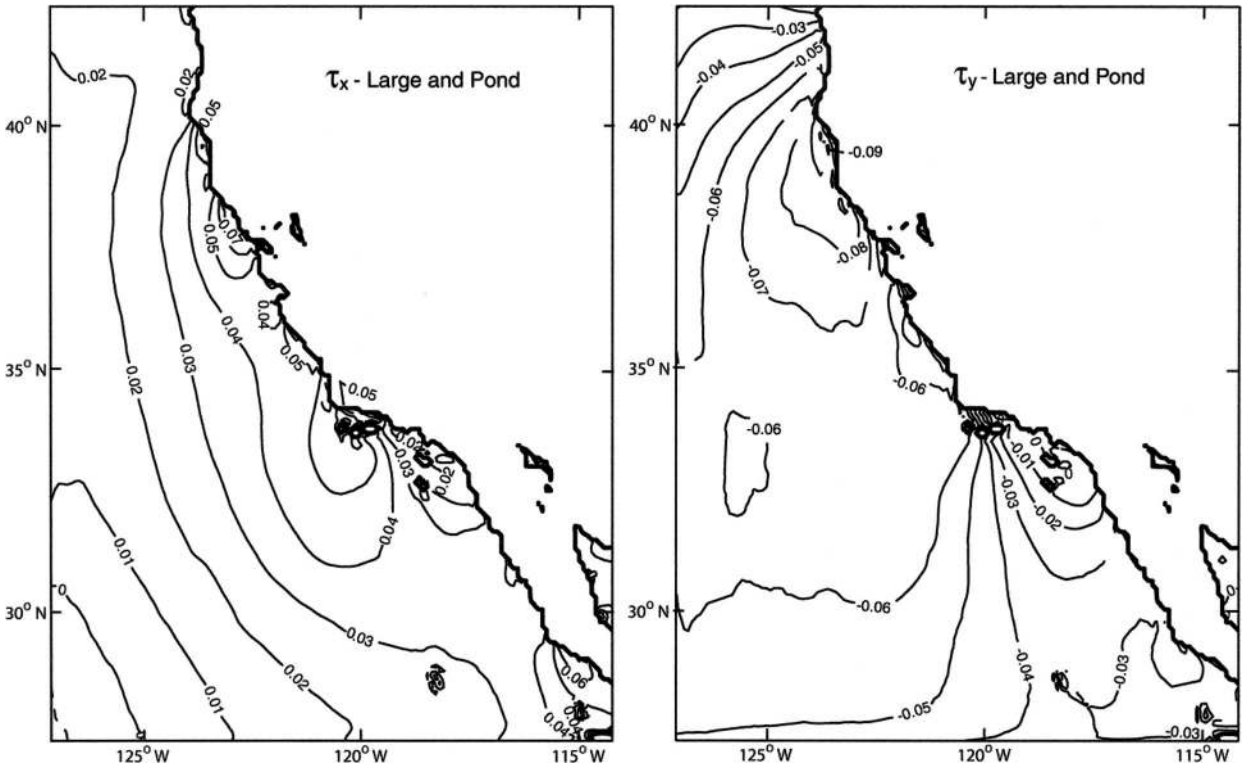

FIG. 12. Averaged (left) τ_x and (right) τ_y wind stress components (Pa) for all of Jun 1999 calculated using MM5 simulated winds with the Large and Pond algorithm. The wind stress components are consistent with the schematic models in Fig. 11.

Arena and Cape Mendocino on 25 June (Figs. 13i–l). The strongest positive wind stress curl field is in the island lees and to a lesser extent in some nearshore areas along northern California (Fig. 13l). In this case, the strongest winds and wind stress are coincident with the strongest trough height and thermal gradients at 500 and 850 hPa that extend from the north only part way into northern California (37°N). According to Fig. 13, great pattern variations occur in the surface winds and wind stress over the scale of days while wind stress curl only experiences small-scale changes.

The limited time span of this study and synoptic conditions restrict conclusions about synoptic relationships. The June 1996 all-California speed maximum is usually associated with an 850-hPa trough over the coast with the axis just inland, which is also the dominant situation for the month. During the six cases when an E–W-oriented ridge extended across northern California, five cases were associated with a northern California wind maximum. The four occurrences of the southern central California/Point Conception area maximum were all associated with a deep, 850-hPa trough approaching from the NW, although this was really one 4-day event.

Table 3 presents the June 1999 occurrence of three basic high wind speed patterns: maxima along northern California, southern California/Point Conception, and all of California in addition to none. The MM5 wind field at 0000 UTC on each day was used to determine the wind speed pattern based upon the 8, 10, and 12 m s^{-1} isotach lines. For the 8 m s^{-1} area, all central California and northern California zones are nearly equal in occurrence and account for all but two days of June. The greater isotach decreases in appearance and shifts to northern California.

The MM5-simulated point wind speed maximum is almost always close to the coast in the lee of a major cape (Table 4). The northern California cape lees dominate with no statistically significant difference among them. The southern California capes trail the northern with half the number of occurrences. If one unusually high speed reading at Point Conception is discounted, the range and maximum values for all capes are similar. Thus, the point of absolute maximum is in a larger, high-speed area that tends to be in northern California.

In summary, wind and wind stress have great structural variability during the month associated with midlevel synoptic fields. In contrast, wind stress curl exhibits less spatial variation. The most prominent areas of positive wind stress curl are the Santa Barbara Channel and island lees. Narrower, near-coast, and much more variable bands of positive wind stress curl are simulated in the lees of northern California capes.

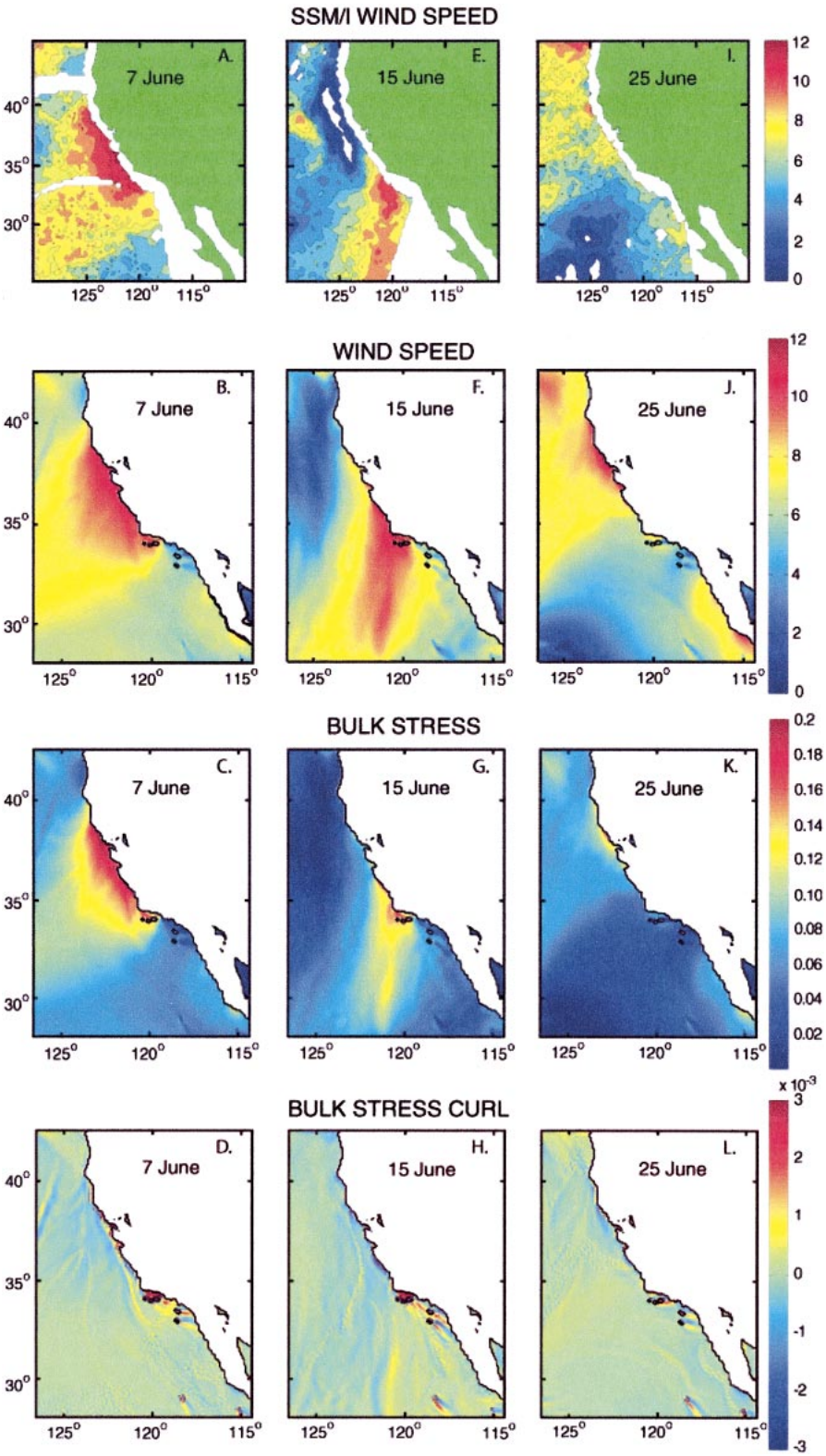

FIG. 13. (top) SSM/I satellite-derived surface wind speed (m s^{-1}) and simulated (2d row) surface wind (m s^{-1}), (3d row) wind stress (Pa), and (bottom) wind stress curl (Pa km^{-1}) for (left) 7, (center) 15, and (right) 25 Jun. All valid near 0000 UTC except for the 15 Jun satellite data, which are near 1600 UTC.

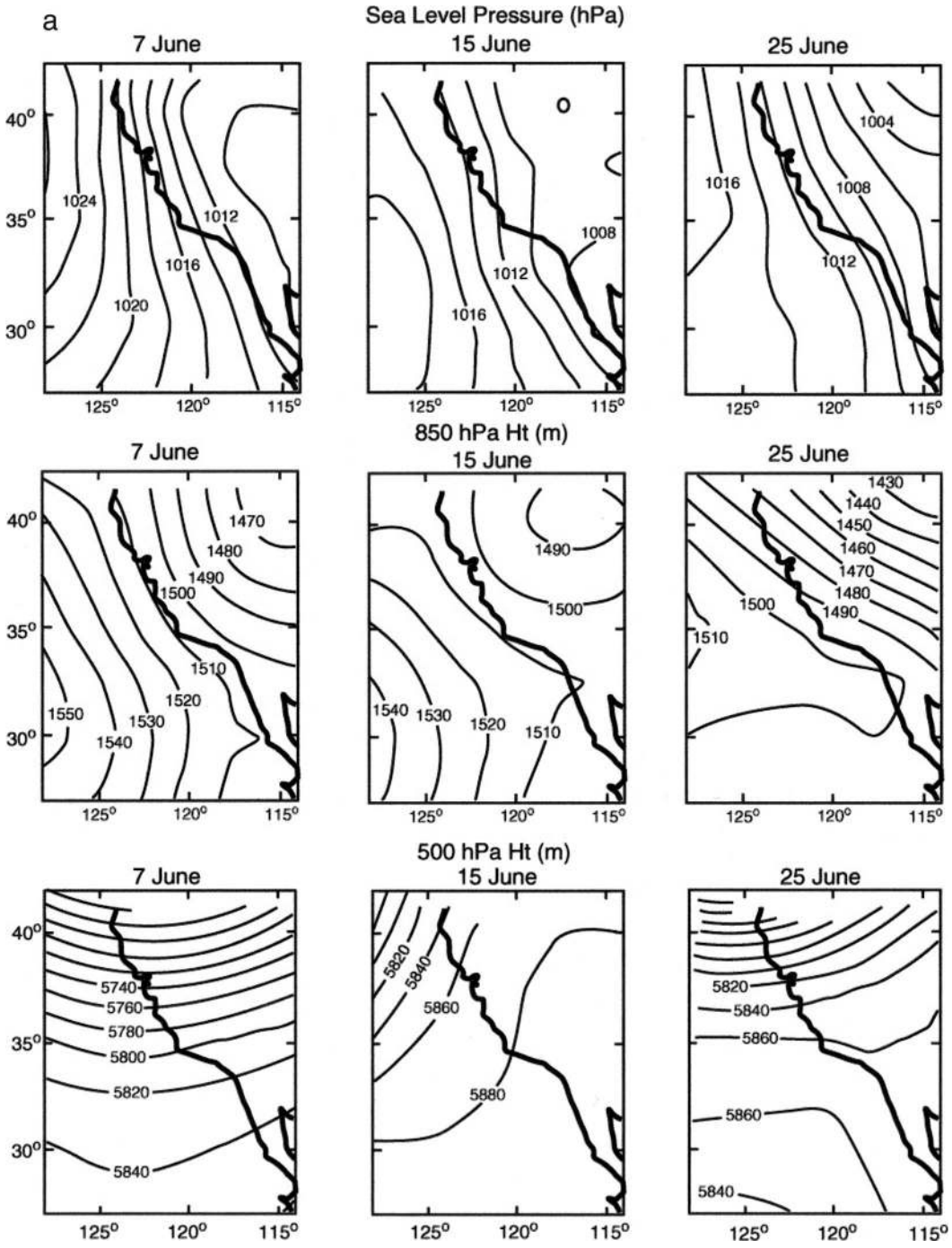

FIG. 14. (a) Analysis of (top) sea level pressure (hPa) and (middle) 850- and (bottom) 500-hPa geopotential height (gpm), valid at the same times and orientation as in Fig. 13. Synoptic analysis is modified from NOAA–Cooperative Institute for Research in Environmental Sciences Climate Diagnostics Center analyses. Large-scale, surface pattern changes are related to midlevel, synoptic changes.

8. Effects of wind stress variability and wind stress curl on ocean dynamics

The model results show three significant features. The strongest upwelling-favorable winds are found between Cape Mendocino and Point Reyes (Figs. 5, 6, and 8). The model also generates two persistent wind stress curl patterns from expansion fans associated with the capes (Fig. 10). There is a narrow band of positive wind stress curl confined to within approximately 20 km of the coast

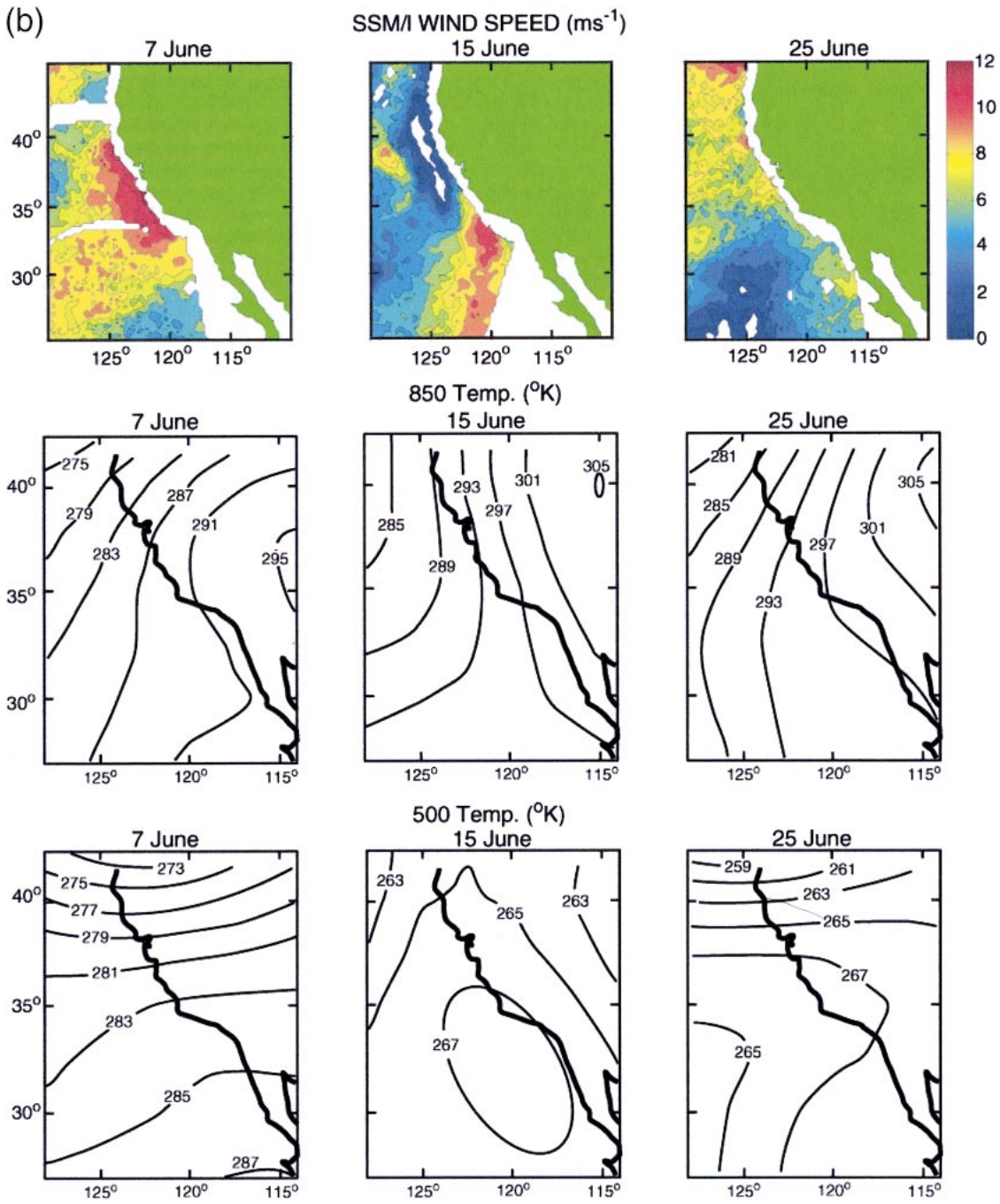

FIG. 14. (*Continued*) (b) (top) SSM/I satellite-derived surface wind speed (m s^{-1}), and analyses of air temperature at (middle) 850 and (bottom) 500 hPa (K).

TABLE 3. Characterization of daily wind speed maximum pattern along California for Jun 1999 at 0000 UTC.

MM5 contour	Northern California	South-central California, Point Conception	All California	None
8 m s^{-1}	11	4	13	2
10 m s^{-1}	7	1	4	18
12 m s^{-1}	2	0	0	28

(Fig. 10a) and a much larger area of positive wind stress curl in the lee of Point Conception (Fig. 10b). What effects could these patterns have on wind-driven upwelling and is there any evidence for these types of effects?

Like in the smaller expansion fans found at many of the capes along the California and Oregon coasts, the large-scale increase in wind speed between Cape Men-

TABLE 4. MM5 maximum wind location for Jun 1999 at 0000 UTC, which almost always occurs in the lee of a cape and close to the coast. A single event is counted twice if two maxima are within 0.5 m s^{-1}.

	Cape Mendocino	Point Arena	Point Sur	Point Conception	Other
No. of cases	13	13	7	6	1
Mean (m s^{-1})	12.5	11.7	12.5	13.4	—
Range (m s^{-1})	9.9–14.2	8.6–13.4	11.1–13.6	11.3–17.5	—

docino and Point Reyes (Fig. 6) may result from an expansion fan associated with the large-scale change in the coastline orientation (Edwards et al. 2002). This along-coast variation in wind stress strength is likely to contribute to increased coastal upwelling between Cape Mendocino and Point Reyes. Satellite sea surface temperature (SST) estimates and surface buoys provide evidence of increased upwelling and decreased near-surface temperatures. Kelly (1985) examined the spatial and temporal structure of SST images and buoy wind measurements for the northern California coast between April and July 1981. The SST temporal mean showed a temperature minimum between Cape Mendocino and Point Reyes. Sea surface temperature variability was analyzed using empirical orthogonal functions (EOFs). Of the three SST EOFs discussed, the first was associated with seasonal warming, while the second corresponded to increased temperature variability between Cape Mendocino and Point Reyes. The second was significantly correlated with wind stress variability in a way consistent with increased winds and coastal upwelling in this area. Buoy temperatures analyzed by Dorman and Winant (1995) also show evidence of increased upwelling between Cape Mendocino and Point Reyes. Average summer buoy temperatures in this region were 10°–11°C as compared with temperatures near 14°C south of Point Reyes and north of Cape Blanco, Oregon.

In addition to the large-scale increase in wind stress between Cape Mendocino and Point Reyes, there is a narrow coastal band (Figs. 10a–c) of positive wind stress curl all along the coast. This band would tend to reinforce coastal upwelling caused by adjustment of the cross-shelf Ekman transport to the presence of the coast. To compare curl-driven upwelling to coastal upwelling it is instructive to form a crude estimate of the scale of the coastal upwelling vertical velocity. For a spatially uniform wind stress (and two-dimensional coastline and bathymetry), coastal upwelling is confined to the region between the inner shelf and midshelf. Over the inner shelf, there is top-to-bottom momentum transfer imparted by the wind stress. This reduces the wind-driven, cross-shelf transport from the theoretical Ekman transport. Over the midshelf, surface and bottom boundary layers are distinct, and surface transport approaches the Ekman transport. Between the inner shelf and midshelf, the divergence in cross-shelf, wind-driven surface transport provides the traditional mechanism for upwelling. The transition between the inner shelf and midshelf is not at a fixed location or depth but rather depends on stratification and bottom slope. Over the northern California shelf, evidence suggests the transition generally occurs somewhere between the 30-m isobath, which is well within the inner shelf (Lentz 1994), and the 90-m isobath where the surface and bottom boundary layers are almost always distinct (e.g., Dever 1997). These isobaths are generally within 20 km of the coast. This horizontal scale and the Ekman transport forced by coastal wind stress provide an estimate of upwelling caused by an adjustment of cross-shelf transport to the coastal boundary.

For two-dimensional volume balance,

$$\frac{du}{dx} = -\frac{dw}{dz}, \tag{4}$$

where u is cross-shelf velocity, x is cross-shelf direction, w is vertical velocity, and z is vertical direction. Integrating from the base of the mixed layer, $-h$ to 0, yields

$$\frac{dU}{dx} = -w(-h) \tag{5}$$

since vertical velocity at the surface is 0. Here U is the surface cross-shelf transport, U at the midshelf is the Ekman transport, and U at the inner shelf is 0. Crudely, Δx is the distance over which adjustment from the inner shelf to the midshelf occurs and is about 10 km:

$$-\frac{1}{\rho f}\frac{\Delta \tau_y}{\Delta x} = w(-h), \tag{6}$$

where τ_y is along-shelf wind stress, ρ is ocean density, f is the Coriolis acceleration, Δx is the scale over which the surface transport goes from zero to the full Ekman transport, and w is the vertical velocity at the base of the surface boundary layer, $-h$. For $\tau_y = -0.1$ Pa, $\rho = 1.025$ kg m^{-3}, $f = 9 \times 10^{-5}$ s^{-1}, and $\Delta x = 10^4$ m, $w = 10^{-4}$ m s^{-1} or 10 m day^{-1}.

Surface divergence (upwelling) caused by the coastal band of positive wind stress curl occurs over the same scales (roughly within 20 km of the coast) as upwelling caused by adjustment of the wind-driven, cross-shelf transport to the presence of the coast. Its magnitude is given by the wind stress curl shown in Fig. 10a. The upwelling velocity caused by wind stress curl, C, in the nearshore positive wind stress is mainly caused by the surface Ekman transport divergence associated with the y component of wind stress. Upwelling velocity at the base of the mixed layer is given by $C(\rho f)^{-1}$. For the range of curl $C = 1$–5 ($\times 10^{-3}$ Pa km^{-1}), with ρ and f as above, the upwelling velocity w is in the range of 1–5 ($\times 10^{-6}$ m s^{-1}) or 0.1–0.5 m day^{-1}. Thus, on monthly

averaged time scales, this model results imply that the coastal wind stress curl effect is secondary but not insignificant.

On event time scales, both wind stress and wind stress curl deviate significantly from the monthly average. The relative importance of coastal boundary upwelling and curl-driven upwelling tends to be similar to that noted above, however. This is because, as the wind stress in a given region increases, the curl near the coast also increases. For example, on 7 June (Fig. 13), both bulk stress and curl along the coast are about double their monthly averages. This cannot be confirmed, however, as direct observations of surface Ekman transport divergence are lacking for the short (20 km) scales of coastal wind stress curl suggested by the June 1999 averages.

Some support for the importance of wind stress curl in forcing ocean dynamics is found in recent model results. Off Oregon, Oke et al. (2002) found evidence of the importance of wind stress variability by considering a numerical model that included data assimilation of observed surface currents. The model was forced by time-varying, spatially uniform winds but incorporated a correction term through data assimilation. The spatial structure of the correction term and its correlation with wind forcing led Oke et al. (2002) to conclude that the correction term was associated with unresolved spatial variability in the wind stress. The cross-shelf structure of the correction term was remarkably consistent with the spatial structure of the wind field predicted by a high-resolution numerical model (Samelson et al. 2002).

Aircraft measurements also indicate that coastal wind stress curl could be important, perhaps more important than suggested by this model. Enriquez and Friehe (1995) considered a simple ocean model forced by wind stress curl consistent with aircraft observations over the northern California shelf. To isolate the effects of wind stress curl variability from bathymetry, they used a 1.5-layer model with an active surface layer and a quiescent bottom layer. For the wind stress curl values considered, they found that wind stress curl could more than double the upwelling over the uniform wind stress case. It is important to note that the wind stress curl values they used were based on aircraft measurements and were up to 10 times the monthly average curl values generated by this model. Besides the difference in the time periods, one significant reason for this difference may be the model's comparatively large grid spacing (9 km) in comparison with the aircraft's effective horizontal-scale resolution (on the order of 100 m). This limited the scales over which the wind stress curl could be calculated.

In addition to the narrow band of positive wind stress curl, there is a larger area of positive wind stress curl associated with the change in coastline orientation at Point Conception (Figs. 10a,b and 11c). Over the Santa Barbara Channel, positive wind stress curl has been observed in aircraft measurements. Over the Southern California Bight, positive wind stress curl is observed in satellite wind measurements (Fig. 13) and in seasonal averages of shipboard measurements. The effects of this positive wind stress curl have been considered in the Santa Barbara Channel and in the greater Southern California Bight. Münchow (2000) averaged aircraft-derived estimates of the wind stress curl in the Santa Barbara Channel and concluded that the wind stress curl could drive Ekman pumping velocities of 4 m day^{-1}. He also concluded that this Ekman pumping may have a role in setting up a cyclonic circulation cell in the western Santa Barbara Channel. As with the work of Enriquez and Friehe (1995), the curl values calculated by Münchow (2000) included scales smaller than the scales we used. In the Santa Barbara Channel, Dever (2004) objectively mapped current and wind fields from moored time series. There was some qualitative agreement between a region of positive wind stress curl south of Point Conception and a collocated upwelling area, but uncertainty estimates precluded more testing to establish quantitative agreement. Recently, Oey (2002) compared model results in the Santa Barbara Channel forced by coarse-scale winds with those forced by higher-resolution winds and concluded the more realistic winds were critical to model performance. On the Southern California Bight scale, Bray et al. (1999) considered the effects of a seasonally averaged wind stress curl (Winant and Dorman 1997) on circulation. Bray et al. (1999) found some evidence that the seasonal regional wind stress curl could drive the seasonal circulation in the Southern California Bight, either through Ekman pumping caused by positive wind stress curl or by the Sverdup balance. They concluded, however, that the observations were an inadequate test of these mechanisms and that a model capable of including unsteady forcing would be a better tool.

9. Summary and conclusions

This study shows that winds, wind stress, and wind stress curl are significantly perturbed along California and Baja California in the upwelling season. The numerical simulations show dominant spatial inhomogeneity and temporal variation of wind and wind stress near the coast with maxima in the lees of major capes near the coastline. This variation results from the influence of coastal topography, geometry of the coastline, and synoptic conditions. While winds and wind stress exhibit significant structure on both the regional scale and mesoscale, positive upwelling-favorable wind stress curl appears to be significant on smaller scales and is confined generally to a narrow band near the coastline and in the island lees. Oceanic surface cross-shelf transport responds to wind forcing on time scales from days to more than one month (e.g., Dever 1997). Our model results demonstrate the wind stress and wind stress curl variability over similar time scales. Hence, wind variability has a strong likelihood of affecting cross-shelf transport and upwelling.

The comparison among buoy 46047 data, SSM/I measurements, and MM5 simulations indicates that model results and satellite measurements show similar wind speeds while both underestimate buoy-measured winds. Differences between observations and model results are caused by many factors but particularly model resolution and the nature of grid-averaged numerical solutions, model assumptions, simplifications, inaccuracies in physical parameterizations, and satellite minimum detection area (footprint) versus buoy spot measurement.

Both satellite-derived and modeled monthly averaged wind speeds show an intense wind maxima along the northern California coast and a broad area of high winds downwind to the Point Conception area. This area of increased wind marks the California regional-scale lee. Both model and satellite show weak winds in the southeastern California Bight and secondary wind maxima in northern Baja California. The region of increased wind stress maps the area of increased wind with maximum stress in the lees of major capes. In both the areas of Cape Mendocino/Point Arena and the Santa Barbara Channel, the maximum hourly wind stress computed from simulations is in excess of 0.32 Pa. In the offshore region of the modeling domain, the maximum wind stress is generally around 0.15 Pa. This large-scale variability likely drives increased coastal upwelling and accounts for the along-shelf minima in sea surface temperatures historically observed between Cape Mendocino and San Francisco.

In the areas where the coastline extends north–south and the prevailing wind and wind stress are southward, wind stress curl is weakly negative westward (in the offshore direction) and strongly positive eastward (toward the coastline) of the location of the maximum wind and wind stress. As a consequence, most of the California coastal waters appear to be under the influence of weak negative wind stress curl.

In the areas where the coastline turns eastward and the dominant northerly flow is channeled, the interplay of spatial variations of wind and wind stress components in the X and Y directions generate positive wind stress curl. The area with the most intense positive wind stress curl is simulated for the western side of the California Bight where the coastline alignment changes by 90°. This curvature effect causes both of the gradient terms in the wind stress curl calculation to be positive and contributes to the high positive value.

Day-by-day analysis of simulations and observations shows that winds and wind stress significantly vary both spatially and temporally; however, the upwelling-favorable positive wind stress curl is persistently confined to a narrow coastal band within about 20 km of the northern California shore and to a broad patch extending more than 100 km offshore in the Southern California Bight.

The coastal positive wind stress curl band occurs in the same area as the active upwelling forced by adjustment to the coastal boundary condition. The wind stress generated by these model simulations indicates that curl-driven upwelling is secondary to boundary-driven upwelling but is not negligible, with curl-driven upwelling being about 5% of the boundary-driven upwelling for the monthly averaged wind stress curl. This estimate of curl-driven upwelling is likely to be a lower bound given the limitations in model resolution (9 km) and curl values computed from aircraft measurements on an event basis and limited area. The larger-scale positive wind stress curl in the lee of Point Conception is qualitatively similar to the curl patterns derived from satellite data and ship observations. There is strong evidence to suggest that this positive curl affects circulation in the Santa Barbara Channel and the Southern California Bight.

Acknowledgments. The study has been supported by DOI-MMS Cooperative Agreement 14-35-0001-30571, and NSF COOP Project Grant OCE-9907884. One of the authors (DK) also acknowledges partial support from DOD–DEPSCoR–ONR Grant N00014-00-1-0524. Mr. Travis McCord and Mr. Domagoj Podnar provided great help in the technical preparation of the manuscript. Mister Roger Kreidberg is acknowledged for editorial assistance.

REFERENCES

Beardsley, R. C., C. E. Dorman, C. A. Friehe, L. K. Rosenfeld, and C. D. Winant, 1987: Local atmospheric forcing during the coastal ocean dynamics experiment. I. A description of the marine boundary layer and atmospheric conditions over a northern California upwelling region. *J. Geophys. Res.,* **92,** 1467–1488.

——, A. G. Enriquez, C. A. Friehe, and C. A. Alessi, 1997: Intercomparison of aircraft and buoy measurements of wind and wind stress during SMILE. *J. Atmos. Oceanic Technol.,* **14,** 969–977.

Beg Paklar, G., V. Isakov, D. Koračin, V. Kourafalou, and M. Orlić, 2001: A case study of bora-driven flow and density changes on the Adriatic shelf (January 1987). *Cont. Shelf Res.,* **21,** 1751–1783.

Bray, N. A., A. Keyes, and W. M. L Morawitz, 1999: The California current system in the Southern California Bight and the Santa Barbara Channel. *J. Geophys. Res.,* **104,** 7695–7714.

Caldwell, P. C., D. W. Stuart, and K. H. Brink, 1986: Mesoscale wind variability near Point Conception, California, during spring 1983. *J. Climate Appl. Meteor.,* **25,** 1241–1254.

Cui, Z., M. Tjernström, and B. Grisogono, 1998: Idealized simulations of atmospheric coastal flow along the central coast of California. *J. Appl. Meteor.,* **37,** 1332–1363.

Deacon, E. L., and E. K. Webb, 1962: Interchange of properties between sea and air. *The Sea,* M. N. Hill, Ed., Ideas and Observations on Progress in the Study of the Seas, Vol. 1, John Wiley and Sons, 43–87.

Dever, E. P., 1997: Wind-forced cross-shelf circulation on the northern California shelf. *J. Phys. Oceanogr.,* **27,** 1566–1580.

——, 2004: Objective maps of near-surface flow states near Point Conception, California. *J. Phys. Oceanogr.,* **34,** 444–461.

Dorman, C. E., and C. D. Winant, 1995: Buoy observations of the atmosphere along the west coast of the United States, 1981–1990. *J. Geophys. Res.,* **100,** 16 029–16 044.

——, D. P. Rogers, W. Nuss, and W. T. Thompson, 1999: Adjustment of the summer marine boundary layer around Pt. Sur, California. *Mon. Wea. Rev.,* **127,** 2143–2159.

——, T. Holt, D. P. Rogers, and K. Edwards, 2000: Large-scale struc-

ture of the June–July 1996 marine boundary layer along California and Oregon. *Mon. Wea. Rev.*, **128,** 1632–1652.

Dudhia, J., 1993: A nonhydrostatic version of the Penn State/NCAR mesoscale model: Validation tests and simulations of an Atlantic cyclone and cold front. *Mon. Wea. Rev.*, **121,** 1493–1513.

Edwards, K. A., 2000: The marine atmospheric boundary layer during Coastal Waves 96. Ph.D. thesis, University of California, San Diego, 132 pp.

——, A. M. Rogerson, C. D. Winant, and D. P. Rogers, 2001: Adjustment of the marine atmospheric boundary layer to a coastal cape. *J. Atmos. Sci.*, **58,** 1511–1528.

——, D. P. Rogers, and C. E. Dorman, 2002: Adjustment of the marine atmospheric boundary layer to the large-scale bend in the California coast. *J. Geophys. Res.*, **107,** 3213, doi:10.1029/2001JC000807.

Enriquez, A. G., and C. A. Friehe, 1995: Effects of wind stress and wind stress curl variability on coastal upwelling. *J. Phys. Oceanogr.*, **25,** 1651–1671.

——, and ——, 1997: Bulk parameterization of momentum, heat, and moisture fluxes over a coastal upwelling area. *J. Geophys. Res.*, **102,** 5781–5798.

Fairall, C. W., E. F. Bradley, D. P. Rogers, J. B. Edson, and G. S. Young, 1996: Bulk parameterization of air–sea fluxes for Tropical Ocean Global Atmosphere Coupled Ocean–Atmosphere Response Experiment. *J. Geophys. Res.*, **101,** 3747–3764.

Friehe, C. A., R. C. Beardsley, C. D. Winant, and J. P. Dean, 1984: Intercomparison of aircraft and surface buoy meteorological data during CODE 1. *J. Atmos. Oceanic Technol.*, **1,** 79–86.

Haack, T., S. Burk, C. E. Dorman, and D. P. Rogers, 2001: Supercritical flow interaction within the Cape Blanco–Cape Mendocino complex. *Mon. Wea. Rev.*, **129,** 688–708.

Halliwell, G. R., and J. S. Allen, 1987: The large-scale coastal wind field along the west coast of North America, 1981–1982. *J. Geophys. Res.*, **92,** 1861–1884.

Gilhousen, D. B., 1987: A field evaluation of NDBC moored buoy winds. *J. Atmos. Oceanic Technol.*, **4,** 94–104.

Grell, G. A., J. Dudhia, and D. R. Stauffer, 1995: A description of the fifth-generation Penn State/NCAR Mesoscale Model (MM5). National Center for Atmospheric Research Tech. Note TN-398, 122 pp.

Jones, I. S. F., and Y. Toba, 2001: *Wind Stress over the Ocean.* Cambridge University Press, 307 pp.

Kelly, K. A., 1985: The influence of winds and topography on the sea surface temperature over the northern California slope. *J. Geophys. Res.*, **90,** 11 783–11 798.

Koračin, D., and C. E. Dorman, 2001: Marine atmospheric boundary layer divergence and clouds along California in June 1996. *Mon. Wea. Rev.*, **129,** 2040–2056.

Large, W. G., and S. Pond, 1981: Open ocean momentum flux measurements in moderate to strong winds. *J. Phys. Oceanogr.*, **11,** 324–481.

Larsen, S. E., M. Yelland, P. Taylor, I. S. F. Jones, L. Hasse, and R. A. Brown, 2001: The measurement of surface stress. *Wind Stress over the Ocean*, I. S. F. Jones and Y. Toba, Eds., Cambridge University Press, 155–180.

Lentz, S. J., 1994: Current dynamics over the northern California inner shelf. *J. Phys. Oceanogr.*, **24,** 2461–2478.

Mellor, G. L., and T. Yamada, 1974: A hierarchy of turbulence closure models for planetary boundary layers. *J. Atmos. Sci.*, **31,** 1791–1806.

Münchow, A., 2000: Wind stress curl forcing of the coastal ocean near Point Conception, California. *J. Phys. Oceanogr.*, **30,** 1265–1280.

Nelson, C. S., 1977: Wind stress curl over the California current. NOAA Tech. Rep. NMFS SSRF-714, 87 pp. [NTIS PB-272310.]

Oey, L.-Y., 2002: A data-assimilated model of the near-surface circulation of the Santa Barbara Channel: Comparison of observations and dynamical predictions. *Eos, Trans. Amer. Geophys. Union*, **83** (Fall Meeting Suppl.), Abstract OS71F-06.

Oke, P. R., J. S. Allen, R. N. Miller, G. D. Egbert, and P. M. Kosro, 2002: Assimilation of surface velocity data into a primitive equation coastal ocean model. *J. Geophys. Res.*, **107,** 3122, doi: 10.1029/2000JC000511.

Powers, J. G., and M. T. Stoelinga, 2000: A coupled air–sea mesoscale model: Experiments in atmospheric sensitivity to marine roughness. *Mon. Wea. Rev.*, **128,** 208–228.

Rogers, D. P., and Coauthors, 1998: Highlights of Coastal Waves, 1996. *Bull. Amer. Meteor. Soc.*, **79,** 1307–1326.

Rossby, C. G., and R. Montgomery, 1935: The layer of frictional influence in wind and ocean currents. Papers in Physical Oceanography and Meteorology, No. 3, MIT and WHOI, 101 pp.

Samelson, R. M., and Coauthors, 2002: Wind stress forcing of the Oregon coastal ocean during the 1999 upwelling season. *J. Geophys. Res.*, **107,** 3034, doi:10.1029/2001JC000900.

Shafran, P. C., N. L. Seaman, and G. A. Gayno, 2000: Evaluation of numerical predictions of boundary layer structure during the Lake Michigan Ozone Study. *J. Appl. Meteor.*, **39,** 412–426.

Toba, Y., S. D. Smith, and N. Ebuchi, 2001: Historical drag expressions. *Wind Stress over the Ocean*, I. S. F. Jones and Y. Toba, Eds., Cambridge University Press, 35–53.

Wentz, F. J., 1997: A well-calibrated ocean algorithm for Special Sensor Microwave/Imager. *J. Geophys. Res.*, **102,** 8703–8718.

Winant, C. D., and C. E. Dorman, 1997: Seasonal patterns of surface wind stress and heat flux over the Southern California Bight. *J. Geophys. Res.*, **102,** 5641–5653.